Investigation of dense gas effects on transition to turbulence over a flat plate boundary layer

by

Akshar Mandyam Chakravarthy

in partial fulfillment of the requirements for the degree of

Master of Science

in Mechanical Engineering

at the Delft University of Technology,

to be defended publicly on Friday the 21st of September, 2018 at 1:30 PM.

Student number:	4627571	
Project duration:	December 1, 2017 – September 21, 2018	
Supervisor(s):	Dr. R. Pecnik ,	TU Delft
	Dr. J. Ren ,	TU Delft
	Dr. O. Marxen	University of Surrey
Thesis committee:	Dr. R. Pecnik ,	TU Delft (chair)
	Dr. J. Ren ,	TU Delft
	Dr. ir. M. Pini ,	TU Delft
	Dr. ir. W.P. Breugem ,	TU Delft
	Prof. dr. ir. B.J. Boersma	TU Delft

TU Delft Delft University of Technology

Acknowledgement

The thesis was a result of encouragement from many people, who helped in shaping the work by providing feedback, direction and valuable support. It is with sincere gratitude that I acknowledge their contributions.

I would like to thank Dr. Rene Pecnik. It is due to his availability and his willingness to conduct interesting research that has given me this wonderful opportunity. His constant support and faith in me to outperform and improve has been empowering, leading to a renewed motivation towards research.

I am also grateful to Dr. Jie Ren for the work he has put towards my thesis. He has been an encyclopedia of knowledge with suggestions and ideas for every hurdle. He has constantly made time for my research, by providing valuable inputs and by being a constant check to validate every detail of my work. His kind and welcoming nature has made the thesis a smooth experience.

I extend my gratitude to Dr. Olaf Marxen, for providing the DNS code, without which the research wouldn't be possible. It is because of his timely guidance and his versatile code that the research has progressed forward without any impasse.

I am also thankful to all the master students at P&E room 34-K-1-100 for providing me with a safe space throughout my thesis. It is largely because of them that I have developed a well-rounded personality with an accentuated learning curve.

Lastly, I thank my family and friends for their constant support and encouragement throughout my 2 year MSc program.

"Turbulence is the norm, laminar is the exception"

Abstract

Laminar-turbulent transition (LTT) is the process through which smooth laminar flow transits into chaotic turbulent flow. Investigation of the paths taken to transit into turbulence is a front-runner among other methods followed to characterise turbulent flows. This is of particular importance in aerospace and energy industries for the design of wings and gas turbines. Early research used Linear Stability Theory (LST) to analyse the stability of the flow; with the increase in computational power, Direct Numerical Simulation (DNS) has been developed to solve the flow field entirely. Most of the research on LTT has been centered on ideal fluids with limited focus on the effects of high temperature. The impact of other strong non-ideal effects on LTT such as dense gas effects have not been investigated. This work aims to study the effects of dense gas on LTT for boundary layer flows of toluene over a flat plate.

Flows over a flat plate boundary layer are investigated in 3 stages. First, the base flow is solved for ideal air and non-ideal toluene for 6 different Eckert numbers (Ec). Second, the base flow is provided as an input to solve the eigenvalues of the stability equations for both fluids and each Ec using an in-house `MATLAB` code. The unstable eigenmode is identified and tracked. The growth rates and phase velocities are calculated and compared between ideal air and toluene. Third, DNS simulations are performed using a `FORTRAN` code, to solve the governing equations of compressible flows for different Ec. The simulations are performed on a pre-processed base flow solution, subjected to 2D sinusoidal perturbations forced into the computation domain at the wall. A no-slip and adiabatic wall boundary conditions are applied to the flat plate with a sponge region at the outlet and the top of the computation domain. The growth rates and phase velocities of these perturbations are calculated and validated with the predictions made by LST. Finally, a perturbation energy budget analysis is conducted to study the nature of the unique results obtained.

The LST results show that as Ec number increases, all flows over a flat plate become more stable. For toluene flows, the stabilising effect of increasing Ec is more pronounced and all flows with $Ec > 0.15$ are stable and have no modal instabilities. The results from the DNS simulations validate these predictions from LST and match perfectly in growing conditions, but deviate from one another in stable conditions. The deviation in results are hypothesised to be the contribution of multiple decaying modes to stable behaviour of the flow. Furthermore, perturbation energy budget analysis showed that for $Ec = 0.05$ and 0.10, the spatial growth of perturbations are positive due to a positive production term and negative for $Ec = 0.15$, with a negative production term. The negative production term is attributed to the negative integral of the perturbation profile.

Contents

List of Figures

List of Tables

Nomenclature

Acronyms

Ec	Eckert number
Ma	Mach number
Pr	Prandtl number
Re	Reynolds number
2D	Two-dimensional
3D	Three-dimensional
BZT	Bethe-Zel'dovich-Thompson
DNS	Direct numerical simulations
LST	Linear stability theory
LTT	Laminar-turbulent transitions
NS	Navier-Stokes
ODE	Ordinary differential equation
ORC	Organic rankine cycles
OS	Orr-Sommerfeld
RK	Runge-Kutta
SQ	Squire
TS	Tollmein-Schlichting

Subscripts and Superscripts

$\hat{u}$	Fourier transformed quantity
$u^{'}$	Perturbation of a quantity
u^{*}	Dimensional quantity
u_{∞}	Freestream properties
u_{i}	Imaginary component
u_{r}	Real component
u_{w}	Value at the wall of the flat plate

Symbols

α_{i}	Growth rate
β	Spanwise wave-number
Δt	Time-step of the DNS simulation
δ	Boundary layer thickness
δ_{ij}	Kronecker delta
η	Transformed spanwise coordinate
Γ	Fundamental derivative of gas dynamics
γ	Ratio of specific heats
κ	Thermal conductivity
λ	Second viscosity
μ	Dynamic viscosity
μ_{b}	Bulk viscosity
ν	Specific volume
Ω	Fundamental circular frequency
ω	Frequency of the perturbation
ρ	Density
τ_{ij}	Viscous stress tensor
A_{v}	Amplitude of the perturbation
B	Dimensionless spanwise wavenumber
c	Speed of sound
C_{p}	Specific heat at constant pressure
C_{v}	Specific heat at constant volume
E	Total energy
F	Dimensionless frequency of the perturbation
h	Static enthalpy
l_{0}	Characteristic length scale of the flat plate
P	Pressure
q_{j}	Heat flux vector
R	Universal gas constant
Re_{x}	Local reynolds number
T	Temperature
u	Streamwise velocity
v	Wall normal velocity
w	Spanwise velocity
x	Streamwise coordinate
y	Wall normal coordinate
Z	Compressibility factor
z	Spanwise coordinate
$\mathbf{q}$	Perturbation Vector

Chapter 1

Introduction

Turbulence is considered to be one of the last remaining unsolved puzzles in classical physics and mathematics. This is due to the complex patterns and behaviour of turbulent flows and the **absence of a strong solution** to the Navier-Stokes (N-S) equations[4]. Strong solutions exist for simple and common geometries, but with increasing complexity (both the flow and the geometry) the turbulent flows become more chaotic and progressively unsolvable. The Navier-Stokes (N-S) equations, which completely describe any flow, are complex non-linear differential equations and are inherently difficult to study or solve completely. The solutions to these non-linear equations involve high-order mathematics and are solved numerically using complicated codes at high computational cost. The results are geometry specific and are not easily transferable to different scenarios of the same flow.

Researchers use various methods to characterise a turbulent flow such as large eddy simulations and averaged N-S equations, which utilises turbulence models. These techniques characterise the features of turbulent flows without explaining how they originate. To understand the genesis of turbulence, researchers study the routes to turbulence and in-turn understand the ways through which flows transition from smooth (laminar) behaviour into complex chaotic (turbulent) behaviour or laminar-turbulent transition (LTT)[42]. The mechanisms that trigger transition depend on the flow characteristics including the geometry and various flow parameters. Hence, *complete knowledge over the behaviour of a fluid for any particular case does not guarantee complete knowledge of the behaviour of the fluid in all cases*.

Almost all flows transition to turbulence upon mass acceleration of the flow or more accurately, by increasing the non-dimensional parameter called the Reynolds number (*Re*)[33]. Figure 1.1 shows an image of a horizontal jet of smoke [1]. The flow of smoke is initially smooth and well defined, the flow here is laminar and the region is referred as the **laminar region**. Far away the smoke is distributed and dispersed in the form of swirls and eddies (vortices), the flow here is chaotic and random with no well defined structures. This region is referred as the **turbulent region**. In between the two regions exists a small region where instabilities form, grow and propagate called the **transition region**. This region is highlighted in red in figure 1.1. In the transition region, the instabilities are first generated through mechanisms like Rayleigh-Taylor instabilities [44]. The instabilities grow in space and time to form larger instabilities triggering secondary and tertiary instabilities, increasing both in strength and in number. The instabilities also propagate downstream in this region before breaking into turbulence. This entire process is explained in more detail in section 2.1.

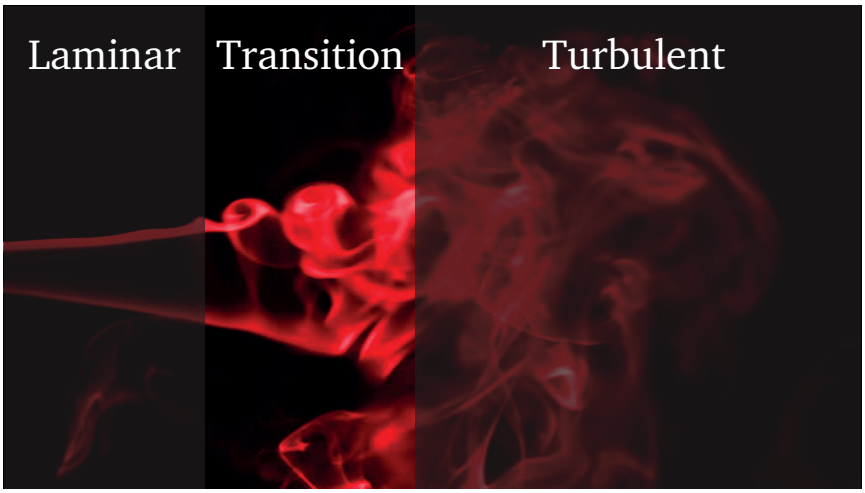

Figure 1.1: Photograph of a horizontal jet of smoke showing the laminar-turbulent transition highlighting the different regions. Red highlights the transition region [1].

An impetus for research on transition stems from the need to delay LTT along the span of an airplane wing [16]. Turbulent flows are the primary cause for drag losses during flight and a delay in transition would **save a large amount of fuel** consumed per flight. With the advancement of science and technology, there is a growing need to understand the effect of real gases on the transition to turbulence for a variety of fluids. Primarily, such focus has been towards high temperature effects in hypersonic boundary layers which is of importance in the aerospace industry. In literature, the high temperature effects have been used synonymously as real gas effects, whereas non-ideal effects encompass the broader range of effects due to compressibility and dense gases among many. These non-ideal effects are explained in detail in chapter 2. The effect of such non-ideal behaviour on LTT can provide crucial input in design of modern gas turbines that use newer fluids such as CO_2 and toluene in supercritical CO_2 cycles and in organic rankine cycles (ORC's) respectively.

1.1 Literature review

The first hypothesis about transition was made by Reynolds who proposed that instabilities are the reason for the transition to turbulence [39]. The hypothesis aimed to explain the observations he made in his famous dye-experiment. This hypothesis was furthered by Rayleigh [35] to establish the initial theory regarding transition to turbulence. Rayleigh assumed an exponential wave-like form for the perturbations and applied them to a linearised inviscid N-S equations to form the *Rayleigh equation*. The solutions proposed by Rayleigh were the first modal approach to solve the instabilities occurring in a fluid flow.

Prandtl, [34] in his lecture at the Third International Mathematics Congress, showed an influence of viscosity near the walls of any boundary, thus hypothesising the boundary layer concept. His students Tollmein [50] and Schlichting [41], furthered the research and theorised that the viscosity near the walls at sufficient Reynolds number induced an alternating grabbing and release of different parallel streams in the flow. This alternating effect translated into simple harmonic oscillations within the boundary layer. These oscillations are referred in literature as *Tollmein-Schlichting (TS) waves*. The waves grow in amplitude downstream and eventually break, to form vortices and eddies typical of a turbulent flow.

Initial wind tunnel experiments could not predict the presence of TS waves. Schubauer and Skramstad [43] noticed that the noise generated in the walls of the wind tunnel could influence the results and is probably the reason why the TS waves could not be detected by previous researchers. They created

a new wind tunnel that limited the noise from the walls. They implemented a vertical array of hot wire anemometers in the boundary layer of the air flow, that substantiated and subsequently captured the simple harmonic variations in velocity that correspond to the theory predicted by Tollmein and Schlichting.

The solutions considered by Rayleigh were for an inviscid fluid. To solve for the viscous flows, a method similar to that used by Rayleigh was used by Orr [32] and Sommerfeld [45]. They solved the divergence of the linearised viscous N-S equations using wave-like perturbations similar to that used by Rayleigh. The final equations derived are referred to as the *Orr-Sommerfeld equations*. This can also be derived by applying a Fourier transform in the x-direction on the linear viscous N-S flow. The solution for the normal velocity will then generate the classical Orr-Sommerfeld equation. Similar to the linearised viscous and invsicid N-S equations, the vorticity equation can be solved applying the procedure assuming a wave-like normal vorticity perturbation. The solutions to the normal vorticity is then given by the *Squire equation* [46]. The solutions of the two equations can be broadly classifed into two types of modes viz. Orr-Sommerfeld modes (OS modes) and Squire modes (SQ modes) solved for different conditions applied to the equations. Depending on whether the domain is bounded or unbounded, the OS modes can have continuous spectrum of modes with finite discrete modes as observed for flows over a flat plate.

Applying Squire transforms to the two equations, it was reported that for every 3D OS mode, there exists a 2D OS mode at a lower Reynolds number. This is referred to as the *Squire's theorem*. This means that for any parallel shear flow, the two-dimensional modes of perturbation become unstable before the three-dimensional modes and have a lower critical Reynolds number than a three-dimensional mode of perturbation. This result is the same for both spatial and temporal problems and is independent of the type of problem being solved. However, Squire's theorem is valid only for incompressible and ideal systems. Supersonic flows at high Mach numbers can have oblique modes of instability where the 2D wave has left the unstable region but some of the transverse waves grow.

Furthermore, in the Orr-Sommerfeld equation, the streamwise wavenumber (α) is part of the non-linear term. This makes the spatial problem non-linear and complicated to solve. Gaster transformation is an useful way to convert the spatial problem into a temporal one that is easier to solve [9]. The Gaster transformation is applicable only for 2D waves and can approximate the relation between temporal and spatial growth rates with good accuracy. This makes it possible to estimate the spatial growth rates from the temporal ones with minimized efforts.

Initially, the theory, solutions and later experiments were performed restricted to simple 2D flows with 2D disturbance fields. 2D flows were further solved assuming the flow within the boundary layer to be parallel. This further reduces the complexity of the problems and thereby the ease in finding the solution. In reality, the growing **boundary layer is not parallel but only quasi-parallel**.

Ling and Reynolds [23] developed a theory for non-parallel effects in incompressible flows with constant viscosity. The study concluded that for self-similar flows, the neutral curve remained unaltered by the non-parallel correction. They also noted that the non-parallel effects were marginal at high Reynolds number. The self-similar solutions are explained in section 2.5.1.

Gaster [10] further studied the stability of small travelling-wave disturbances. He used an iterative method using an asymptotic series solution of the inverse of the Reynolds number raised to power of one half. He observed that at large Reynolds numbers the first two terms of the asymptotic series matched well with experimental data. He concluded that the parallel flow assumptions are valid solution based on the neutral stability boundaries at large Reynolds number.

Such approximations are shown to be valid depending on the geometry and conditions of the flow. Using the numerical solutions provided by Mack [24][25], it was shown that the parallel flow assumption can give adequate results even with higher approximations. Thus, for both Blasius and

Falkner-Skan flows with *high Reynolds number the flows can be assumed to be parallel without any loss in flow behaviour*.

With the growth of research in the field, three dimensional disturbances were also investigated. Dunn & Lin [7] compared the 2D compressible boundary layer subjected to 3D disturbances. They observed that for flows with only viscous-conductive effects the 3D disturbance equations can be transformed into reduced 2D disturbances. The reduced 2D disturbance equation can be solved using the same procedures as other 2D disturbance systems but the reduced 2D disturbance equations do not have a family of solutions.

Gregory et al. [12] and Moore [29] both studied the stability of 3D boundary layers to 3D disturbances for incompressible flows. Their results can be summarised as, " For a disturbance assumed to be moving in a certain direction, the eigenvalue problem may be treated as a two-dimensional one, governed by the boundary-layer velocity profile measured in that direction." Using the analysis provided by Reshotko [37], we can conclude that **this is true even for compressible flow**.

Reshotko [38] also noted in his annual review, that for a thorough understanding of boundary-layer transition process it is essential to take the three-dimensional effects into consideration, especially the upstream initial conditions. Mack [25] compared first-mode disturbances and reported a 10% difference in growth rate between 2D and 3D boundary layers.

In the 1960's an important development was made regarding the supersonic flows in boundary layers. Lees and Reshotko [20] undertook a study of stability of compressible laminar boundary layer taking into the consideration the effects of temperature on viscosity and thermal conductivity. They questioned the uniqueness of the subsonic solution and Mack [25] soon showed using extensive calculations that it is possible for higher modes to exist. Mack referred to these as first mode and second mode of disturbance. Lees and Gold [19] confirmed the conditions for the existence of these additional modes and these higher modes have been experimentally observed in many hypersonic flows.

Real gas effects

Real gas effects in literature deal with flows at high temperature, typically observed in hypersonic flows. Hypersonic flows are characterised by Mach numbers larger than 5, found in problems of atmospheric reentry and other hypersonic flights. At such large Mach numbers, the viscous heating is significant and results in high temperature within the boundary layer. The high temperature can result in the dissociation of air into individual species. The composition of these species change the physics of the flow and need to be accounted during simulation.

Initial experimental studies in hypersonic boundary layers achieved high Mach numbers by decreasing the speed of sound rather than increasing the velocity of the fluid flow. Kendall [17], in his work on zero pressure gradient hypersonic boundary layers, experimentally studied the origins of the natural disturbances occurring in the boundary layers for several Mach numbers between 1.6 to 8.5. It was observed that flow fluctuations originate ahead of the expected region. At higher supersonic velocities these fluctuations were found to be cross-correlated with the sound field. The growth rates observed were in close agreement to the theory predicted by Mack. Demetriades [5] conducted similar experiments but on a sharp cone. It was reported that for flows with Mach number 8 and Reynolds number within the range of $10^6 \leq Re_x \leq 6 \cdot 10^6$ the laminar wave structure broke down. The most intense fluctuations were observed near the boundary layer edge and was found to have higher harmonics suggesting the instabilities to correspond with Mack's second mode.

The above experiments characterise the conditions of flow perfectly. However, by achieving hypersonic flows through decreasing the speed of sound dictates that the kinetic energy of the obtained flows are not comparable in order-of-magnitude with the dissociation energy of the gas. Flows that have large

kinetic energy with high enthalpy and high Mach numbers are also referred to as hypervelocity flows. Studies of hypervelocities were initially conducted solely using numerical methods.

Malik and Anderson [26] performed a linear stability analysis of high temperature boundary layers with an assumption of chemical equilibrium using a *real gas model*. The effects of chemical reactions were introduced only in the mean flow and the variation of the gas properties. Results for Mach 10 and 15 showed that the effects of the real gases were to stabilise the first mode of instability, while it made (Mack's) second mode more unstable. They further reported that the second mode instability shifts to lower frequencies. Stuckert and Reed [47] further showed that, for flows around a sharp cone under both chemical equilibrium and chemical non-equilibrium, the second mode of instability is more unstable for high temperature boundary layers corresponding to Mach number 25. The research also concluded that the second mode became unstable at lower frequencies. Similar results were obtained by other researchers for more complicated models and various boundary condition [15].

With the improvement in measurement techniques and equipment, it was possible to achieve hypersonic flows by increasing the flow velocity leading to a new wave of experimentation and results. Germain and Hornung [11] conducted experiments exploring the transition on a slender cone with hypervelocity flow at zero incidence angle. They used a free-piston shock tunnel T5 with surface heat flux measurement and resonantly enhanced optical visualisation seeded with sodium particles to determine the transition point and identify the boundary layer. They reported that the observed transition mechanism resembled the Tollmein-Schlichting instability. It was also observed that the second mode of instability as predicted by Mack does exist.

Hornung [14] conducted an extensive set of experiments at the T5 high enthalpy shock tunnel and concluded that for hypervelocity flows over a slender cone, both, the relaxation processes of the excitation and dissociation of air can have significant stabilizing effects. The location of transition was evaluated by finding the position at which there was a distinct rise in the heat flux. Further, Hornung observed a significant increase in transition Reynolds number for an increase in the total enthalpy, concluding that **transition is significantly influenced by high enthalpy real gas effects** and establishing that the acoustic instability mode to be the main reason for transition.

The above mentioned research on hypersonic boundary layer is *a precursor to the numerical techniques employed in the direct numerical simulations* conducted in this report.

From the literature review of instability in flows, it is observed that the existing research has focused primarily on ideal fluids and secondarily, on high temperature effects. There is **limited research on the impact of other non-ideal effects, such as the dense gas effects, on laminar-turbulent transition**. These non-ideal effects can change the stability of flows and lead to new behaviour of flows that have not been characterised yet.

1.2 Research motivation

LTT is of particular importance in the energy industry. Identifying the nature of these transition within the turbine of many processes can help achieve a better design and finally lead to an increase in efficiency. However, most of the existing knowledge of LTT is limited to behaviour of ideal or simple fluids. With the advent of new technology, more complex fluid substances are employed. One such important fluid is toluene (C_7H_8), which can be in organic rnakine cycles (ORC's).

An ORC is any ordinary rankine cycle that operates with an organic working fluid like toluene. A Rankine cycle is a closed-loop system where the working fluid goes through a sequence of usually 4 steps viz. isentropic compression, heat addition at constant pressure, isentropic expansion and heat removal at constant pressure. The use of an organic working fluid shifts the two-phase region to lower temperatures. The reduced temperatures of the two-phase region enables the system to work with

low or medium grade source of energy. This makes ORC a primary candidate for many applications like waste heat recovery systems, geothermal plants and solar thermal power plants.

The literature gap identified in the previous section pushes for a need to understand the stability of flows of complex fluids. This is the the primary motivator for the research conducted in the thesis. The research aims for a better understanding how dense fluids like toluene behave during accelerating flows, especially in the stator of the turbine of an organic rankine cycle. As the research in this area is still primitive and in its nascent stage, the work has been conducted for a simple flat plate boundary layer with no pressure gradient.

1.3 Research objective

The research aims to investigate the laminar-turbulent transitions over a flat plate boundary layer for a non-ideal fluid (toluene). This is achieved by initially evaluating the base flow using the self-similar solution. Using the base flow, modal analysis is conducted by evaluating the stability equations and solving for the eigenmodes. Further, the governing equations are solved directly using direct numerical simulations. Finally, The linear stability analysis and the DNS results are validated with each other.

1.4 Thesis outline

Chapter 2 - THEORETICAL FRAMEWORK, introduces the necessary concepts required to understand the basic behaviour of both the fluid and the flow before describing the methods used to investigate the problem.

Chapter 3 - FLOW CONDITIONS AND NUMERICAL CONCEPTS, introduces the operating conditions of the cases simulated along with a brief explanation of the numerical techniques employed in the course of the study to achieve the proposed goals.

Chapter 4 - RESULTS AND DISCUSSIONS, presents the findings from the research conducted for various cases analysed and explains in detail the observations made from the work.

Chapter 5 - CONCLUSIONS, summarises the main outcomes from the research and discusses its significance. It further provides recommendations for future work.

Chapter 2

Theoretical framework

The chapter aims to explain the different concepts and theories required to understand and solve the transition problem for non-ideal flows in a flat plate boundary layer.

2.1 Laminar-turbulent transition

The first chapter gives an understanding of the research interests in LTT. It explains the progress of research in the area as well as the reasons and motivations behind the research. The chapter however, restricted itself to explaining the methods and research behind transition, but does not explain the entire process through which these transitions trigger turbulence, which is explained here.

The transition process often follows multiple paths and can be complicated. These paths have been outlined by Morkovin [30] and are shown in figure 2.1. These paths can be roughly outlined as transition caused by exponential or wave-like disturbances as analysed using linear stability theory (path a and b) or transition through bypass (path d and e). Path a refers to the growth of instabilities due to excitation of the natural modes of the flow, similar to the exponential growth modes observed in Tollmien-Schlichting (TS) mechanism. Path e or the bypass transition refers to the observation made by Morkovin that an alternate amplifying mechanism can make the flow transition into turbulence without encountering the TS mechanism.

The different stages that occur during laminar-turbulent transition are:

- *Receptivity*: Refers to the mechanisms through which forced disturbances enter the boundary layer. This was first introduced by Morkovin [30]. Receptivity analysis says that if the initial disturbances are sufficiently large, the forcing mechanisms within the flow can force the growth mechanism directly into non-linear levels and subsequently into turbulent flow. Alternately, through receptivity analysis, it is shown that if the initial disturbances are small, free disturbances within the boundary layer are triggered. These free disturbances are the normal modes of the boundary layer and are referred to as TS waves for inviscid flows.

- *Linear growth*: Refers to a stage where the small perturbations within the flow start to grow in amplitude until its effects become non-linear and can no longer be adequately described in a linear manner.

  The growth of a disturbance can be modal, as in the exponential growth of an eigenmode or can be the non-modal by forcing disturbances on the fluid.

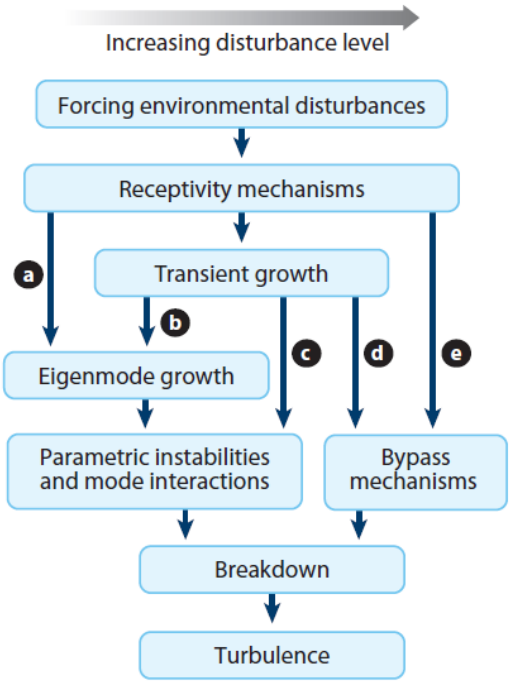

Figure 2.1: Different paths of laminar to turbulent transition [8]

- *Non-linear saturation*: In this stage, the perturbations within the flow have all reached a particular amplitude such that the disturbances have saturated and the flow reaches a new steady state of a more complicated flow. The new complex flow acts as the new base flow upon which the secondary instabilities can grow.

- *Secondary instability*: Refers to the new instabilities created within the more complex flows that grow and propagate throughout the flow field. The instabilities in this region exhibit rapid growth and are more complex than the linear growth instabilities.

- *Breakdown*: This is the last stage of transition into turbulence, where the flow truly becomes chaotic, a fundamental characteristic of turbulent flows. Within this region the non-linear instabilities rapidly increase in number and excite even more frequencies within the flow.

2.2 Flat plate boundary layer

Prandtl [34], first hypothesised that fluids adhere to the wall of solids. This small region near the wall where the effects of viscosity are visible is referred to as the boundary layer. Figure 2.2, shows the boundary layer over flat plate which is the most common type of boundary layer.

Assume a fluid of uniform flow field (u_∞), entering the region above a flat plate as shown in figure 2.2. Close to the flat plate the fluid particles adhere to the particles of the wall, resulting in no relative motion between the two. This concept is referred as the *no-slip condition*. The cohesive forces (viscosity) between the fluid particles ensures that the layers above the plate are prevented from moving freely. This dragging of subsequent layers of the fluid flow lead to the formation of a velocity profile (u) close to the flat plate. The influence of the wall stops when the velocity profile reaches the value of the free stream (u_∞). As the fluid flows downstream, the fluid layer adhering to the wall

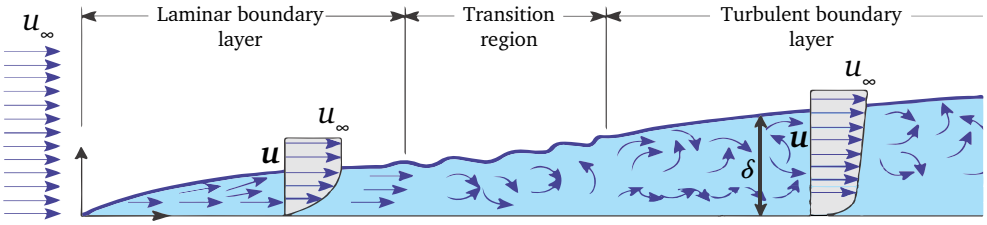

Figure 2.2: Boundary layer for a flow over a flat plate showing the regions of importantance.

boundary has more time to influence the layers above it, leading to an increase in the thickness of the boundary layer (δ). In practice the thickness of the boundary layer is defined to be the distance from the wall where the velocity of the fluid reaches 99 % of the freestream value.

The concept of boundary layer explained with respect to the velocity is called the *velocity boundary layer*, and is more commonly used in literature. The same theory can be applied to temperature as well giving the *thermal boundary layer*.

The boundary layer is very smooth close to the leading edge. The velocity profiles are rounded in shape and the streamlines within the boundary layer are quasi-parallel. Such a boundary layer is called a **laminar boundary layer** and such boundary layer structures are highly sought after in most designs of aerofoils as they have the least drag. At larger distances from the leading edge, the structures of the laminar boundary layer develops instabilities that propagate and grow in space and time. The boundary layer in this region is not well defined and the streamlines are no longer smooth. This correspond to the **transition region**. At even larger distances, the instabilities generated in the transition region breaks down to form a new boundary layer with flatter velocity profiles and vortices. This is referred to as the **turbulent boundary layer**.

2.3 Real gas effects

Toluene (C_7H_8) is a substance that shows a strong non-ideal behaviour as a superheated vapour close to the vapour saturation line [48]. These behaviours can be broadly characterised by two important properties of the fluid viz. compressibility factor (Z) and fundamental derivative of gas dynamics (Γ).

The compressibility factor is defined as the ratio of molar volume of a gas to the molar volume of an ideal gas at the same temperature and pressure. It is an indicator of the **accuracy of assumptions of ideal gas**. A value of $Z = 1$ represents an ideal gas. Any value apart from unity suggests a significant contribution of the size of each molecule of the gas and/or the degree of interaction between these particles.

The fundamental derivative of gas dynamics classifies the behaviour of toluene based on its complexity owing to its dense molecular composition. Compressible flows within the dense gas regime follow a different relation between the speed of sound and the change in density. Γ is defined as:

$$\Gamma \equiv 1 + \frac{\rho}{c}\left(\frac{\partial c}{\partial \rho}\right)_s = 1 + \frac{\rho}{2c^2}\left(\frac{\partial^2 P}{\partial \rho^2}\right)_s = \frac{v^3}{2c^2}\left(\frac{\partial^2 P}{\partial v^2}\right)_s, \tag{2.1}$$

where $v = 1/\rho$ is the specific volume and the speed of sound is defined as $c^2 = (\partial P/\partial \rho)_s$.

Based on the value of Γ, the behaviour of any fluid can be categorised into 3 different regions.

- $\Gamma > 1$: This region is the most common category found among gases. Such behaviour is typical for all ideal and simple molecule gases encountered in day to day life such as water vapour, CO_2 etc. For an ideal gas Γ is given by the relation $\Gamma = (\gamma+1)/2$, where γ

is the ratio of specific heats (C_p/C_v). For all ideal gases the value of γ is always greater than unity and hence the value of Γ is always greater than 1.

A value of Γ greater than unity means that the value of $(\partial c/\partial \rho)_s$ is always positive. This means that the **speed of sound in the gas increases upon compression**. Also, a value of $\Gamma > 0$ signifies that the value of $(\partial^2 P/\partial v^2)_s$ is also positive, which is the usual form of the inequality assumed to study shock wave properties.

- $0 < \Gamma < 1$: A value of $\Gamma < 1$ corresponds to negative value of the partial derivative $(\partial c/\partial \rho)_s$. The negative value is a consequence of the dense gas properties of toluene and other similar gases. The negative value of the partial derivative signifies that for the dense gas an **increase in density at isentropic conditions is accompanied by a reduction in the speed of sound**.

  This leads to a non-monotonic change in the speed of sound for the fluid resulting to non-monotonic change in the Mach numbers. Such fluid behaviour does not necessarily lead to adverse effects on the shock wave but could influence the features of the shock wave. As in the previous category, the value of Γ is greater than 0. Thus the partial derivative $(\partial^2 P/\partial v^2)_s > 0$. Hence the gas shows a normal variation in properties across a shock wave.

- $\Gamma < 0$: The gases that belong to this region exhibit different properties in comparison with ideal gases. These fluids are called Bethe-Zel'dovich-Thompson (BZT) fluids in recognition of the studies conducted by the three scientist who theorised the existence of such fluids along with the likely properties they would possess. BZT fluids experience a larger decrease in the speed of sound upon compression and vice-versa in comparison with the dense fluids mentioned in the previous category. The large decrease in speed of sound upon compression can lead to sensitive behaviour of the fluid around shock waves. BZT fluids also obey the partial derivative $(\partial^2 P/\partial v^2)_s < 0$ which enables them to possess certain unique qualities such as the permissibility of rarefaction waves [52] [49]. Theoretically, this could allow for fluids that do not generate shocks upon expansion which is very ideal for a working fluid in a turbine. Typical BZT fluids include very large hydrocarbons. The benefits of BZT fluids are plentiful along with its difficulties which are not discussed in the report.

2.4 Research methodology

The methodology adopted to achieve the objective of the thesis is summarised in figure 2.3. The different steps followed are:

1. First, the governing equations are derived. An order-of-magnitude analysis is performed to simplify the governing equations and obtain the self-similar equations. The solutions of the self-similar equations are computed using properties given in an 1D look-up table to obtain the base flow (green boxes).
2. Second, the governing equations are subjected to a perturbation analysis to obtain the stability equations, which are solved with the base flow as input giving the LST results (blue boxes).
3. Third, the governing equations are completely solved by the DNS solver. The solver computes the solutions over a pre-processed base flow, using properties from the 2D look-up table (red boxes). The DNS and LST results of growth rate (α_i), phase velocity (c) and perturbation vector ($\hat{q}$) are compared with one another.

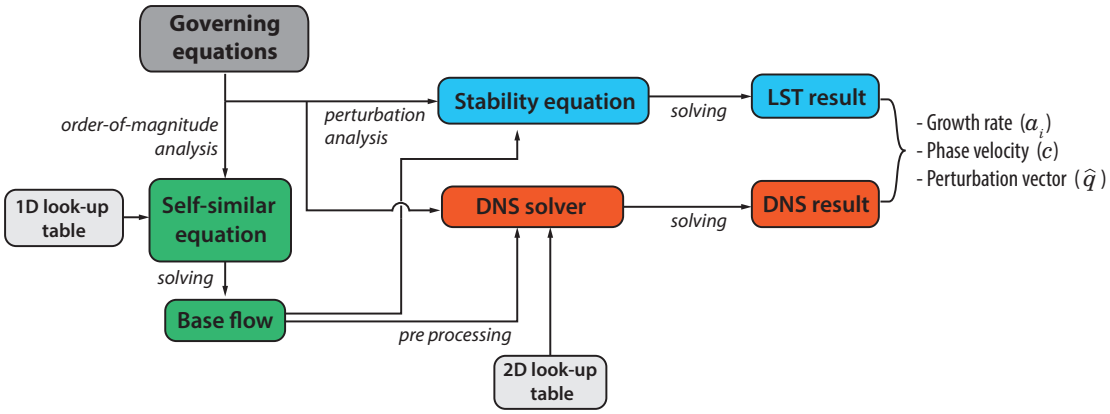

Figure 2.3: Summary of the methods followed in the thesis.

2.5 Governing equations

The flow over a flat plate can be characterised using the laws of conservation of mass, momentum and energy which together are called the Navier-Stokes equations and individually as the continuity equation (2.2), momentum equation (2.3), and energy equation (2.4) given as:

$$\frac{\partial \rho}{\partial t} + \frac{\partial (\rho u_j)}{\partial x_j} = 0, \tag{2.2}$$

$$\frac{\partial (\rho u_i)}{\partial t} + \frac{\partial (\rho u_i u_j + p\delta_{ij} - \tau_{ij})}{\partial x_j} = 0, \tag{2.3}$$

$$\frac{\partial (\rho E)}{\partial t} + \frac{\partial (\rho E u_j + p u_j + q_j - u_i \tau_{ij})}{\partial x_j} = 0. \tag{2.4}$$

The equations (2.2)-(2.4) are dimensionless and follow the general Einstein notations. In the equation, $x_i = (x, y, z)$ indicating the streamwise, wall-normal, and spanwise directions, $u_i = (u, v, w)$ are the corresponding velocity components. t is time, ρ is the density of the fluid, p is the pressure and $E = e + \frac{1}{2}u_i u_i$ is the total energy of the fluid with e being the internal energy. The viscous stress tensor (τ_{ij}) and the heat flux vector (q_j) are given as:

$$\tau_{ij} = \frac{\mu}{\mathrm{Re}}\left(\frac{\partial u_i}{\partial x_j} + \frac{\partial u_j}{\partial x_i}\right) + \frac{\lambda}{\mathrm{Re}}\delta_{ij}\frac{\partial u_k}{\partial x_k}, \tag{2.5}$$

$$q_j = -\frac{\kappa}{\mathrm{Re}\,\mathrm{Pr}\,Ec}\frac{\partial T}{\partial x_j}.$$

The two terms in the viscous stress tensor (τ_{ij}) physically signify the stress generated due to change in shape and change in volume, respectively. Here, μ is the dynamic viscosity and $\lambda = \mu_b - 2/3\mu$ is the second viscosity with μ_b denoting the bulk viscosity. In all of the results presented henceforth, the bulk viscosity is assumed to be zero. The heat flux vector (q_j) is an indicative of the amount of heat that is distributed in each direction with κ being the thermal conductivity.

The N-S equations are non-dimensionalised using the scaling and reference values given by:

$$u = \frac{u^*}{u^*_\infty},\ x_i = \frac{x^*_i}{l^*_0},\ t = \frac{t^* u^*_\infty}{l^*_0},\ p = \frac{p^*}{\rho^*_\infty {u^*_\infty}^2},\ \rho = \frac{\rho^*}{\rho^*_\infty},$$
$$T = \frac{T^*}{T^*_\infty},\ E = \frac{E^*}{{u^*_\infty}^2},\ \mu = \frac{\mu^*}{\mu^*_\infty},\ \kappa = \frac{\kappa^*}{\kappa^*_\infty}. \tag{2.6}$$

The scaling adopted are routine steps with each quantity being normalised with their values in the free-stream, except time which is scaled with l^*_0/u^*_∞, Energy with ${u^*_\infty}^2$ and pressure with $\rho^*_\infty {u^*_\infty}^2$. The subscript '$\infty$' represents free-stream values and superscript '*' represents dimensional quantities.

Scaling analysis are a mainstay to solving problems in fluid dynamics and result in the formation of dimensionless quantities of significant importance or *similarity parameters* as used by certain authors. For the flow of a compressible non-ideal fluid over a flat plate boundary layer the most important parameters are the Reynolds number(Re), Prandtl number(Pr), Eckert number(Ec) and the Mach number (Ma). Each parameter is defined as:

$$Re_\infty = \frac{\text{inertial forces}}{\text{viscous forces}} = \frac{\rho^*_\infty u^*_\infty l^*_0}{\mu^*_\infty}, \tag{2.7}$$
$$Pr_\infty = \frac{\text{viscous difusion rate}}{\text{thermal diffusion rate}} = \frac{\mu^*_\infty C^*_{p\infty}}{\kappa^*_\infty}, \tag{2.8}$$
$$Ec_\infty = \frac{\text{kinetic energy}}{\text{enthalpy}} = \frac{{u^*_\infty}^2}{C^*_{p\infty} T^*_\infty}, \tag{2.9}$$
$$Ma_\infty = \frac{\text{velocity}}{\text{speed of sound}} = \frac{u^*_\infty}{c^*_\infty}. \tag{2.10}$$

In the above equations, l^*_0 is a chosen length scale, c^*_∞ is the speed of sound in the free-stream. Also Eckert number for an ideal gas is given as $Ec_\infty = (\gamma - 1)Ma^2_\infty$, where γ is the ratio of specific heat capacity.

The dimensionless quantities mentioned in equations (2.7)-(2.10) characterise the behaviour of the flow completely, i.e. two flows having the same value for all the dimensionless quantities are similar. The corollary suggests that changing any or all of these quantities effectively changes the dynamics of the flow.

The physical significance of each of these similarity parameter is as follows;

- The Reynolds number (Re) is defined to be the ratio of inertial forces with respect to the viscous force. It is a measure of the importance of viscosity over a flow. Large values of Re indicate flows which do not depend significantly on the viscosity of the fluid in the free-stream. Typically, increasing the Reynolds number causes the flow to transit into turbulence.

- The Prandtl number (Pr) is the ratio of momentum and thermal diffusivity. In boundary layers, it also gives a comparison between the velocity and thermal boundary layers. For example $Pr > 1$ signifies that at any streamwise location the velocity boundary layer is thicker than the thermal boundary layer.

- The Eckert Number (Ec) is defined to be the ratio of kinetic energy and the enthalpy. It is a measure of how the heat is dissipated in high speed flows, where the contribution of viscous dissipation is important.

- The Mach number (Ma) is the ratio of local velocity and the speed of sound in the medium. The dimensionless number is an indicator of the compressibility of the flow. In reality, every flow is compressible to some extent, but upto Ma=0.3 the effects of compressibility can be assumed to be negligible.

The N-S equations (2.2)-(2.4) are solved completely using a computation technique called direct numerical simulation (DNS). Before solving the complete N-S equations, the base flow is first computed as an initial solution. Thereafter, the base flow is used as input for stability analysis and DNS.

2.5.1 Laminar base flow

The Blasius solution or the self-similar solution over a flat-plate is chosen as the base flow and henceforth will be used interchangeably. The self-similar solution acts as the initial state (base flow) for the LST and DNS perfomed in this work.

The exact solution to the N-S equations are hard to calculate and possible today only due to the advent of computational fluid dynamics. These computational techniques are accurate, but are computationally heavy and for a large part of the 20th century, a simpler viscous flow equation was derived by relevant order-of-magnitude reduction to form the boundary layer equations. Blasius [3] was the first to propose such a boundary layer equation for a flat plate in the year 1908.

The N-S equations given in equations (2.2)-(2.4) are subjected to a routine order-of-magnitude analysis. Let us first consider a flat plate of length 'l' and boundary layer thickness δ, the primary assumption in boundary layer theory is to consider the thickness of the boundary layer to be very small in comparison with the length of the plate, i.e.

$$\delta << l. \tag{2.11}$$

The 2D compressible continuity equation is given as:

$$\frac{\partial(\overline{\rho u})}{\partial \overline{x}} + \frac{\partial(\overline{\rho v})}{\partial \overline{y}} = 0. \tag{2.12}$$

The above equation is non-dimensional and scaling each of the quantities appropriately, we find that $v = O(\delta)$ as given in the following:

$$\frac{[O(1)][O(1)]}{O(1)} + \frac{[O(1)][\overline{v}]}{O(\delta)} = 0. \tag{2.13}$$

Further, the x-momentum equation is considered and the orders of each term is calculated to check for terms that can be neglected, giving the following:

$$\overline{\rho u}\frac{\partial \overline{u}}{\partial \overline{x}} + \overline{\rho v}\frac{\partial \overline{v}}{\partial \overline{y}} = -\frac{1}{\gamma M_\infty^2}\frac{\partial \overline{p}}{\partial \overline{x}} + \frac{1}{\mathrm{Re}_\infty}\frac{\partial}{\partial \overline{y}}\left[\overline{\mu}\left(\frac{\partial \overline{v}}{\partial \overline{x}} + \frac{\partial \overline{u}}{\partial \overline{y}}\right)\right], \tag{2.14}$$

$$\overline{\rho u}\frac{\partial \overline{u}}{\partial \overline{x}} = O(1) \qquad \overline{\rho v}\frac{\partial \overline{v}}{\partial \overline{y}} = O(1) \qquad \frac{\partial \overline{p}}{\partial \overline{x}} = O(1), \tag{2.15}$$

$$\frac{\partial}{\partial \overline{y}}\left(\mu\frac{\partial \overline{v}}{\partial \overline{x}}\right) = O(1) \qquad \frac{\partial}{\partial \overline{y}}\left(\mu\frac{\partial \overline{u}}{\partial \overline{y}}\right) = O\left(\frac{1}{\delta^2}\right). \tag{2.16}$$

From the above equations we can obtain an order-of-magnitude equation as:

$$O(1)+O(1)=-\frac{1}{\gamma M_\infty^2}O(1)+\frac{1}{\mathrm{Re}_\infty}\left[O(1)+O\left(\frac{1}{\delta^2}\right)\right]. \tag{2.17}$$

To resolve the order of magnitude analysis, we make another assumption that the Reynolds number is large, such that its inverse scales with the square of the boundary layer thickness, given as:

$$\frac{1}{Re}=O(\delta^2). \tag{2.18}$$

The assumption gives the order of the term $(1/Re)\partial/\partial\bar{y}(\bar{v}\partial\bar{v}/\partial\bar{x})=O(\delta^2)$. Using the first assumption (equation (2.11)) δ is small, therefore the square is even smaller and hence can be neglected. Similar comparison of order of magnitude can be conducted on the y-momentum and in the energy equation to get the final compressible boundary layer equation (BLE) given as following:

$$\frac{\partial(\rho u)}{\partial x}+\frac{\partial(\rho v)}{\partial y}=0, \tag{2.19}$$

$$\rho u\frac{\partial u}{\partial x}+\rho v\frac{\partial v}{\partial y}=-\frac{\mathrm{d}p_e}{\mathrm{dx}}+\frac{\partial}{\partial y}\left(\mu\frac{\partial u}{\partial y}\right), \tag{2.20}$$

$$\frac{\partial p}{\partial y}=0, \tag{2.21}$$

$$\rho u\frac{\partial h}{\partial x}+\rho v\frac{\partial h}{\partial y}=\frac{\partial}{\partial y}\left(k\frac{\partial T}{\partial y}\right)-u\frac{\mathrm{d}p_e}{\mathrm{dx}}+\mu\left(\frac{\partial u}{\partial y}\right). \tag{2.22}$$

The above equations are subjected to the boundary conditions as follows:

At the wall:

$$y=0,\quad u=0,\quad v=0,\quad \left(\frac{\partial T}{\partial n}\right)_w=0.$$

At the boundary edge:

$$y\to\infty,\quad u\to u_\infty,\quad T\to T_\infty.$$

The boundary edge is not fixed for all positions along the x direction and hence it is calculated at the limit y=∞.

Self-similar solutions

The main idea behind the self-similar solution is illustrated in figure 2.4. The velocity profile of the flow is a function of both x and y coordinates. Thus, for 2 different positions in streamwise direction, $u(x1,y1)\neq u(x2,y2)$. This is depicted in the figure, where the red and blue profiles calculated with the physical scale of x and y at 2 different x value do not match. The profiles can be appropriately modified to a transformed scale of ξ and η, where the two variables ξ and η are independent and chosen such that the velocity profile is no longer dependent on the location. This is shown in the figure 2.4 in the transformed scale, where the red and blue profiles match.

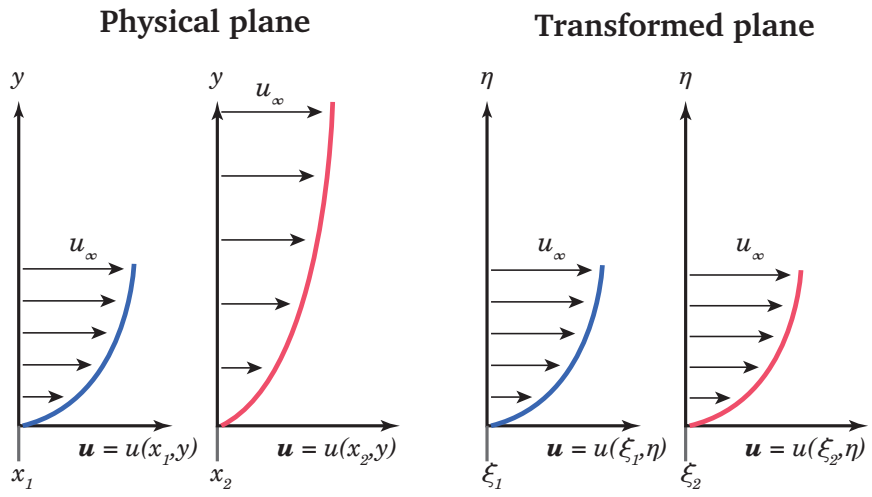

Figure 2.4: Illustration of the concept of self-similarity.

The transformed variables suitably change the velocity profiles to make it independent of the transformed surface distance and become a function of only one variable i.e. $u = u(\eta)$. This property earns the right for such boundary layers to be called *self-similar boundary layer* and the solutions for such boundary layers to be referred to as *self-similar solutions*.

The appropriate transformations chosen are based on the work by Dorodnitsyn[6] in the 1940's and later refined by Levy [22] and Lees[18]. These transformations are referred to as Lees-Dorodnitsyn transformation as used by Anderson Jr [2] given as following:

$$d\xi = \rho_\infty \mu_\infty u_\infty dx, \tag{2.23}$$

$$d\eta = \frac{\rho u_\infty}{\sqrt{2\xi}} dy. \tag{2.24}$$

The process of finding the self-similar solution typically follows four steps viz.

1. Transformation of the independent variables: Here the derivatives in x and y are replaced with derivatives in ξ and η.
2. Transformation of the dependent variables: A function $f(\xi, \eta)$ is defined such that the partial derivative of f with respect to η is defined to be the normalised velocity profile. i.e.

$$\frac{u}{u_\infty} = \frac{\partial f}{\partial \eta} \equiv f'.$$

3. Finding a correlation between f and the stream function ψ.
4. Obtain the final transformed equation.

Following the above process we get the final self similar boundary layer equation given as:

$$\begin{aligned} (C_l f'')' + f f'' &= 0, \\ \left(\frac{C_l}{\mathrm{Pr}_l} g'\right)' + f g' + C_l \frac{{u^*_\infty}^2}{h^*_{t\infty}} (f'')^2 &= 0. \end{aligned} \tag{2.25}$$

In equation (2.25), h_t is the static enthalpy and the local variables are given as:

$$f' = \frac{u^*}{u^*_\infty}, \quad g = \frac{h^*_t}{h^*_{t\infty}}, \quad C_l = \frac{\rho^*\mu^*}{\rho^*_\infty\mu^*_\infty}, \quad Pr_l = \frac{\mu^* C^*_p}{\kappa^*}. \tag{2.26}$$

The local variables are functions of η alone and independent of ξ.

The final self similar boundary layer equations (equation (2.25)) are **a set of ordinary differential equations** (ODE's) making analytic solutions easier to calculate. These ODE's are numerically integrated using the *fourth-order Runge-Kutta (RK-4)* scheme with adiabatic wall boundary condition.

A 1D look-up table is used to help with the calculation of various parameters given in the boundary layer equations. The look up table is generated using the `Fluidprop` library by calculating values of different thermodynamic properties for different temperatures at constant pressure. These properties are later used by the code to relate g, C_l and Pr, finally providing an estimation of the thermodynamic and transport properties of the flow generating the laminar base flow. The look-up table is presented in appendix A.1.

2.6 Linear stability theory

Linear stability theory is a concept applied to fluid mechanics to understand modal instabilities similar to the research conducted by Rayleigh and Taylor. With the growth of computational methods and ease of numerical simulations, The solutions to the modal problem can be numerically computed faster in comparison with its analytic solution. The solution computed in this report are numerical using an in-house code developed by Ren et al. (2018).

Linear stability analysis assumes that when a flow is perturbed, **all modes of perturbation are excited, but only a few modes grow in space and/or time while the other modes decay**. The unstable modes are identified and its behaviour is tracked over the flow domain. Perturbation analysis decomposes the variables as a sum of a mean and perturbation given as:

$$\begin{aligned}
\rho &= \rho_0 + \rho' \\
u_i &= u_{i,0} + u'_i \\
T &= T_0 + T' \\
p &= p_0 + p' \\
E &= E_0 + E' \\
\mu &= \mu_0 + \mu' \\
\kappa &= \kappa_0 + \kappa'
\end{aligned} \tag{2.27}$$

For a simple compressible system, any thermodynamic state can be completely defined using any two independent intensive property. In this study, the density ρ and temperature T of the fluid are chosen as the basic thermodynamic properties. All other transport and thermodynamic properties are calculated as a function of these independent properties.

Each variable within the N-S equation is substituted with the decomposition given in equation (2.27) and then subtracted with the base flow equations. The resulting equation is linearised, i.e the non-linear terms are neglected and we get the stability equation given as:

$$\begin{aligned}\mathbf{L_t}\frac{\partial \mathbf{q}}{\partial t}+\mathbf{L_x}\frac{\partial \mathbf{q}}{\partial x}+\mathbf{L_y}\frac{\partial \mathbf{q}}{\partial y}+\mathbf{L_z}\frac{\partial \mathbf{q}}{\partial z}+\mathbf{L_q}\mathbf{q}\\ +\mathbf{V_{xx}}\frac{\partial^2 \mathbf{q}}{\partial x^2}+\mathbf{V_{xy}}\frac{\partial^2 \mathbf{q}}{\partial x \partial y}+\mathbf{V_{xz}}\frac{\partial^2 \mathbf{q}}{\partial x \partial z}+\mathbf{V_{yy}}\frac{\partial^2 \mathbf{q}}{\partial y^2}+\mathbf{V_{yz}}\frac{\partial^2 \mathbf{q}}{\partial x^2}+\mathbf{V_{zz}}\frac{\partial^2 \mathbf{q}}{\partial z^2}=0.\end{aligned} \tag{2.28}$$

Here, $\mathbf{q}=(\rho', u', v', w', T')^T$ is the perturbation vector and the complete expression for the matrices $\mathbf{L_t}$, $\mathbf{L_x}$, $\mathbf{L_y}$, $\mathbf{L_z}$, $\mathbf{L_q}$, $\mathbf{V_{xx}}$, $\mathbf{V_{yy}}$, $\mathbf{V_{zz}}$, $\mathbf{V_{xy}}$, $\mathbf{V_{yz}}$ and $\mathbf{V_{xz}}$are provided in detail in Ren et al. [36]. The perturbations are assumed to be exponential of the form:

$$\mathbf{q}(x,y,z,t)=\widehat{\mathbf{q}}(y)\exp(i\alpha x+i\beta z-i\omega t)+c.c\ . \tag{2.29}$$

In the above equation, α is the streamwise wavenumber, β is the spanwise wavenumber, ω is the frequency of the perturbation and $c.c$ is the complex conjugate. The above perturbation vector is unstable if the exponential is negative i.e if the value of α or β are negative or if ω is positive. Substituting equation (2.29) in equation (2.27) we get the eigenvalue problem.

The stability equation can either be solved as a temporal problem, where the perturbations grow in time, or a spatial problem, where the perturbations grow in space. For boundary layer problems, it is common to solve the spatial problem with a prescribed spanwise wave number β and frequency ω.

The equations are discretised using the Chebyshev points and Chebyshev differentiation matrix and solved with the boundary condition: $u'=v'=w'=\partial T'/\partial y=0$ at the wall (y=0) and $u'=v'=w'=T'=0$ in the freestream ($y\to\infty$).

The stability equation is solved for the entire domain and the eigenvalues and corresponding eigenvectors are calculated. The unstable mode, if any, is identified and the growth rate and phase velocity of the mode is observed for different frequencies and streamwise position.

2.7 Direct numerical simulation

Direct numerical solutions refer to the technique of completely solving the N-S equations, by solving the entire temporal and spatial scales i.e both the macro and micro scales of the flow. It is a technique used very often in turbulence to resolve the entire flow but is used here to solve the flow field using the self-similar solution as the base flow.

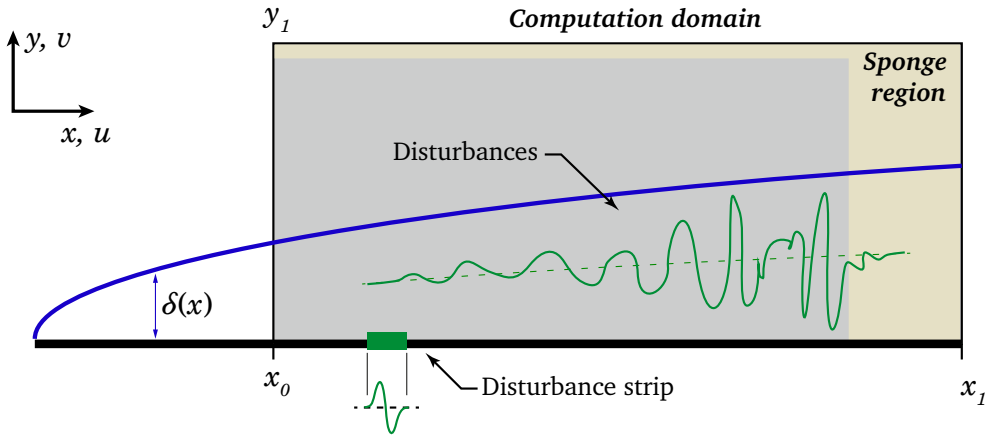

Figure 2.5: Illustration of the computation domain used in direct numerical solutions. The region within the box represents the computational domain and the region in yellow represent the sponge region. The boundary layer is given as a blue curve and the disturbances are plotted as green curves.

Figure 2.5, gives a description of the domain of the DNS problem. The flow is solved within the computational domain indicated by the box ranging from x_0 to x_1 in the streamwise direction and from 0 to y_1 in the wall normal direction. Disturbances are introduced into the computational domain using a suction/blowing strip (*Disturbance strip*) at the wall of the flat plate. The disturbances (*green curves*) grow within the computational domain according to modal analysis. The grey region depicts the actual region where the 2D disturbances are calculated and the yellow region to the top and right of the domain represents the sponge region. In the sponge region or the re-laminarisation zone, the solution calculated by the DNS is damped to the base flow (indicated by the flattening of the disturbances).

The equations are discretised using *a third-order Runge-Kutta scheme in time with staggered arrangement of variables and a sixth order compact finite difference scheme in space*. The entire flow field is represented as a 2D space of ρe and e. The various properties are calculated using a 2D look-up table created using `fluidprop`. The 2D table is a matrix of values of different properties as a function of internal energy e and density ρ. More details regarding the table can be found in appendix A.2. The numerical concepts and ideas employed in solving the DNS as well as the base flow and LST are explained in detail in chapter 3.

Chapter 3

Numerical concepts and flow conditions

The chapter consists of a description of the numerical techniques applied in simulating the LTT across the flat plate. The code used in the research has been developed by adapting an in-house code for linear stability analysis written in `MATLAB` and an external DNS code written in `FORTRAN`. Further, the operating conditions for toluene and variation of some important properties are explained using temperature-entropy ($T-s$) diagrams.

The code used as part of the LST was implemented by Dr. Jie Ren, Postdoc at Process and Energy Laboratory of TU Delft. The description of the code used is provided in Ren et al. [36]. The DNS code was written by Dr. Olaf Marxen, Lecturer at the University of Surrey as part of his PhD research. More details of the code can be found in the research papers by Marxen et al. [27] [28].

3.1 Numerical concepts of base flow

The base flow as explained in section 2.5.1, refers to the solution of the self-similar boundary layer equations. The flow is completely governed by the Eckert number and Reynolds number with the Mach number dependent on the Eckert number. Prandtl number for flows with constant reference pressure and temperature is also fixed. For all simulations made in the report, the Reynolds number has been fixed at 10^5 and the Eckert number is varied for each case for both ideal air as well as toluene.

The system of ODE in equation (2.25) are only a function of a single variable (η) and is numerically integrated using a fourth-order Runge-Kutta 4 scheme (RK-4), this takes the form of a simple Simpson integral:

$$f_{n+1} = f_n + \frac{1}{6}(k_1 + 2k_2 + 2k_3 + k_4), \tag{3.1}$$

with each individual terms defined as:

$$k_1 = f(t_n, y_n)dy,$$

$$k_2 = f\left(t_n + \frac{1}{2}, y_n + \frac{k_1}{2}\right)dy,$$

$$k_3 = f\left(t_n + \frac{1}{2}, y_n + \frac{k_2}{2}\right)dy,$$

$$k_4 = f(t_n + 1, y_n + k_3)dy.$$

The values of different transport and thermodynamic properties are taken from the 1D property table described in appendix A.1. The 1D table is input to a FORTRAN code that solves for the laminar base flow on a uniform rectangular grid composed of typical rectangular boundary layer cell with an equidistant spacing in the streamwise (x) direction with 800 (MX) points and a stretching applied in the wall normal direction (y) according to the formula:

$$y(1,m) = y_1\left((1-k)\left(\frac{m-1}{MY-1}\right)^3 + k\,\frac{m-1}{MY-1}\right). \tag{3.2}$$

In the above stretching formula, $k = 0.25$, and m = 1...MY. The stretching can be made equidistant by adjusting k to unity. This stretching allows the boundary layer to be better resolved in comparison with the freestream to capture the physics within the boundary layer more accurately.

The output of the base flow is stored as binary files in a plot3d format with data of both the thermodynamic and transport properties.

3.2 Numerical concepts of LST

The linear stability theory solves the stability equations given in equation (2.28) using an in-house MATLAB code. The MATLAB program uses Chebyshev points to create the grid in the wall-normal direction (y). The base flow is generated using the new grid and the stability equations are suitably discretised using the Chebyshev differentiation matrices. A full detailed description of the technique can be found in Trefethen [51] and Ren et al. [36].

The stability equations are solved with the transport and thermodynamic properties as a function of temperature and density as previously mentioned. Hence, first and second derivatives of E, P, μ and κ with respect to ρ and T are computed using the base flow as well as the Fluidprop library. The derivatives depend on the non-ideal behaviour of the fluid and are the real gas related terms given in table 3.1. The variation of these derivatives for ideal and toluene directly impact the solution of the LST.

The stability equations are evaluated at an initial value of Re_x and dimensionless frequency (F) such that the flow has a clearly defined unstable mode. The initial estimate chosen during this study is a value of $Re_x = 2000$ and F= 10e-6. The local Reynolds number Re_x, which is a depiction of the streamwise coordinate, the non-dimensional spanwise wavenumber (B) and frequency (F) are defined as:

$$F = \frac{2\pi f^* \mu^*_\infty}{\rho^*_\infty U^{*2}_\infty} = \frac{\omega}{\mathrm{Re}_x}, \quad \text{with} \quad B = \frac{\beta}{\mathrm{Re}_x} \quad \text{and} \quad \mathrm{Re_x} = \sqrt{\mathrm{x}\cdot\mathrm{Re}}. \tag{3.3}$$

Table 3.1: The real gas related terms in stability equation.

Thermodynamic properties	Transport properties
ρ_0, e_0, 0	μ_0, κ_0
$\frac{\partial e_0}{\partial \rho_0}$, $\frac{\partial e_0}{\partial T_0}$	$\frac{\partial \mu_0}{\partial \rho_0}$, $\frac{\partial^2 \mu_0}{\partial T_0}$, $\frac{\partial^2 \mu_0}{\partial \rho_0^2}$, $\frac{\partial^2 \mu_0}{\partial \rho_0 \partial T_0}$, $\frac{\partial^2 \mu_0}{\partial T_0^2}$
$\frac{\partial p_0}{\partial \rho_0}$, $\frac{\partial^2 p_0}{\partial T_0}$, $\frac{\partial^2 p_0}{\partial \rho_0^2}$, $\frac{\partial^2 p_0}{\partial \rho_0 \partial T_0}$, $\frac{\partial^2 p_0}{\partial T_0^2}$	$\frac{\partial \kappa_0}{\partial \rho_0}$, $\frac{\partial^2 \kappa_0}{\partial T_0}$, $\frac{\partial^2 \kappa_0}{\partial \rho_0^2}$, $\frac{\partial^2 \kappa_0}{\partial \rho_0 \partial T_0}$, $\frac{\partial^2 \kappa_0}{\partial T_0^2}$

Solving the stability equations for a particular flow condition results in an eigenspectrum. The eigenspectrum is a constellation of all eigenmodes which are solutions to the stability equation. The solutions corresponding to each mode in the spectrum may not be physical and a few numerical modes are also generated. When the flow is excited, all the physical modes are excited, but only the unstable mode grows making the perturbations applied grow in space.

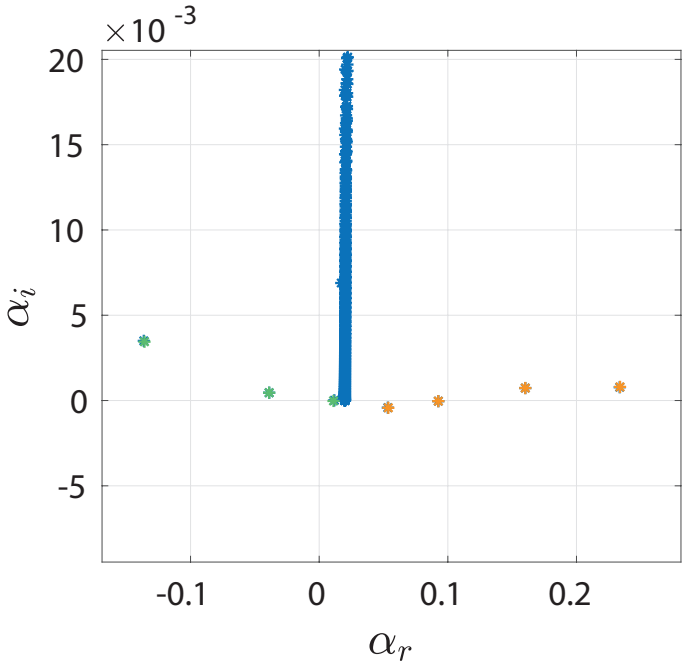

Figure 3.1: Eigenmode spectrum for Ec = 0.10 showing the different continuous modes and discrete modes. (*) indicates slow acoustic modes (mode S), (*) indicates the fast acoustic mode (mode F) and (*) indicates the entropy/vorticity modes.

Figure 3.1, shows a typical eigenspectrum observed for a flow over a flat plate, with α_r on the x-axis and α_i on the y axis. In figure 3.1, each '*' correspond to an eigenvalue. Within the figure, three chains of continuous modes viz. the slow acoustic modes or (mode S) according to Fedorov, fast acoustic mode (mode F) and the entropy/vorticity modes are visible. The mode S eigenmodes (indicated with *) have a phase velocity never exceeding unity, whereas the mode F eigenmodes (indicated with *) have a phase velocity greater than unity which could reduce lower than unity downstream. The entropy/vorticity modes (indicated with *) have a phase velocity exactly equal to unity. The continuous modes are present for all Eckert numbers, but appear closer to each other when the Mach number or alternatively the Eckert number is increased.

Apart from the continuous modes a few discrete modes are also present within the spectrum. The unstable mode is a discrete mode with α_r greater than that corresponding to the entropy/vorticity modes i.e the unstable mode is close to the mode S spectrum, but appears in the 4th quadrant with a negative value of α_i.

Each eigenmode has a corresponding eigenvector or eigenfunction as given in figure 3.2. In the figure, plots of the perturbation as defined in equation (2.29) are made for each of the 5 variables stored at every cell in the computation domain viz. $|\hat{u}|, |\hat{v}|, |\hat{w}|, |\hat{\rho}|, |\hat{T}|$ all normalised with the streamwise velocity in the freestream. Each of the perturbation profile is the absolute value of the Fourier transformed variable.

Once a physical unstable mode is identified it is tracked for Re_x ranging from 0-2000 and F ranging from 0 - 200e-6. The solution computed is stored as a `.mat` file for post-processing.

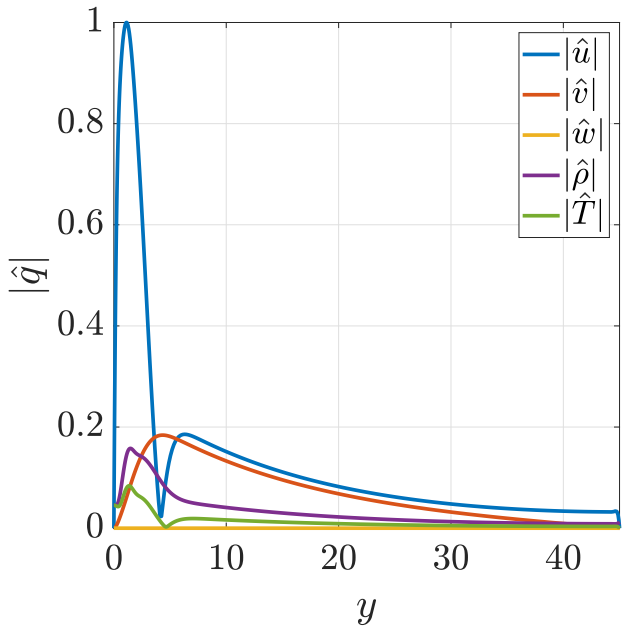

Figure 3.2: Typical eigenfunctions of the unstable mode in the eigenvalue spectrum. Each plot is the absolute value of the Fourier transform.

3.2.1 Post-processing

From the `MATLAB` code, the eigenvalues and eigenvectors of the corresponding eigenmode are available for a range of Re_x and F. The growth rate (α_i) and phase velocity (c) are calculated for each of these modes. The imaginary part of each eigenmode gives the growth rate of the mode and the neutral stability curve of the flow can be plotted using a surface plot as given in figure 3.3.

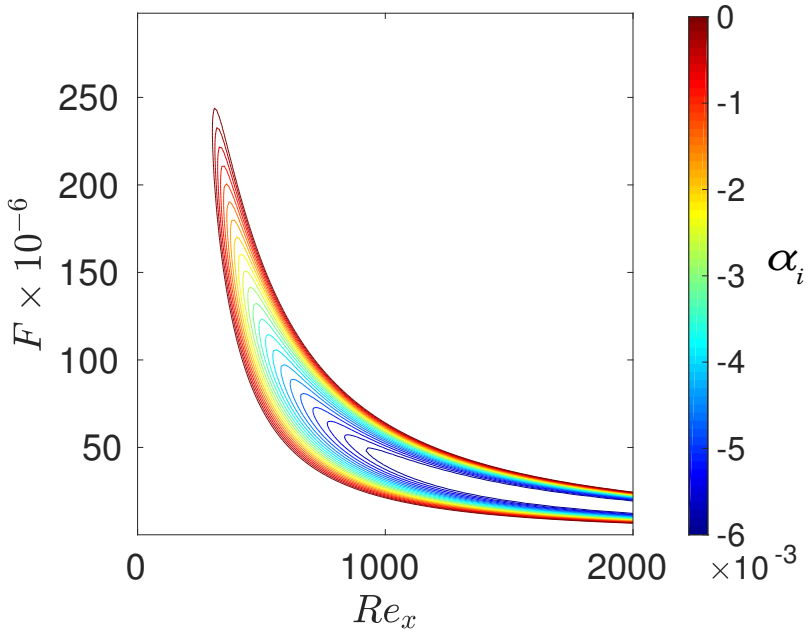

Figure 3.3: Contour plot of growth rate of the perturbation as a function of non-dimensional frequency (F) and local Reynolds number Re_x for $Ec = 0.005$. The outermost contour corresponding to $\alpha_i = 0$, represents the neutral curve.

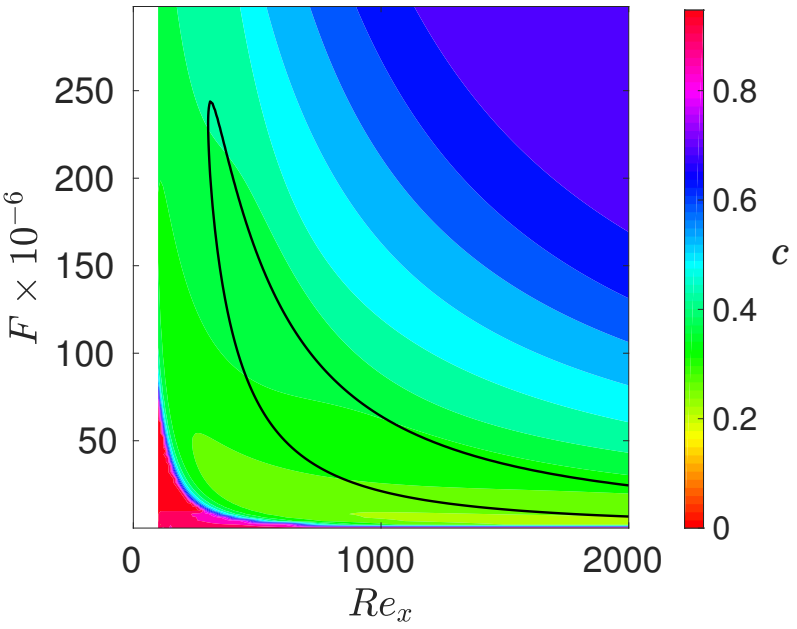

Figure 3.4: Contour plot of variation in phase velocity of the perturbation for $Ec = 0.005$. The solid black line represents the corresponding neutral curve.

The neutral curve given in the figure, is a contour plot of growth rate as a function of dimensionless frequency F in the y-axis and the local Reynolds number Re_x in the x-axis. The range of the growth rate is given in the `colorbar` of the image. The outer curve corresponding to $\alpha_i = 0$, is referred to as the *neutral curve*. The neutral curve separates the unstable and stable region of the flow, with the region within the neutral curve depicting the unstable region and the region more central of the neutral curve is more unstable than the edges.

Similar to the previous contour plot, a plot with contours of phase velocity, defined as $c = \omega/\alpha$, is also plotted (figure 3.4). Such a plot gives an insight into the speed of propagation of the instabilities across the flow. For eg. in the figure it is observed that the perturbations have a phase velocity between 0.2 and 0.4 inside the unstable region.

3.3 Numerical concepts of DNS

The direct numerical simulations do not use the output from the base flow unchanged. The output from the base flow is first pre-processed, before simulated upon. Pre-processing converts the general collocated grid in `plot3d` format generated by the base flow to the format required by the staggered code. It also computes the metrics and writes them in the format required by the staggered code.

During pre-processing, all gas properties are tabulated as a function of internal energy e^* and the product of internal energy and density $\rho^* e^*$. The 2D look up table, explained in appendix A.2, is prepared using `Fluidprop` for a range of e^* and $\rho^* e^*$. During any simulation, the interpolations are first performed for a varying e^* and a constant $\rho^* e^*$ in the neighbourhood of the required $\rho^* e^*$. This procedure provides the dimensional values of each quantity which are non-dimensionalised with their respective reference values.

The pre-processing is executed using a `FORTRAN` code and the pre-processed solutions are stored as binary files which are used later as the inputs to another `FORTRAN` code that solves the governing equations (2.2)-(2.4) with a high-order accuracy. This is achieved by using a staggered Cartesian grid

and a discretisation in space using a 6th order compact difference method and an explicit third-order Runge-Kutta time-stepping [40] [21].

A staggered grid has an arrangement of variables as shown in fig 3.5b. In this arrangement, the velocity and transport properties are calculated at the cell walls and are half a cell width away from the centre of the cell where the thermodynamic quantities are calculated. Such an arrangement was first developed as a solution to the checkboard problem or the decoupling of the pressure and velocity in incompressible flows by Harlow and Welch [13]. Compressible flows usually are solved using collocated grids with an arrangement where all dependent variables are calculated at the same place as shown in figure 3.5a. A study carried out by Nagarajan et al. observed that the staggered grid is more robust than collocated grids. Robustness is the capability of the grid to run simulations of high *Re* with relatively fewer grid points i.e. an under-resolved problem [40].

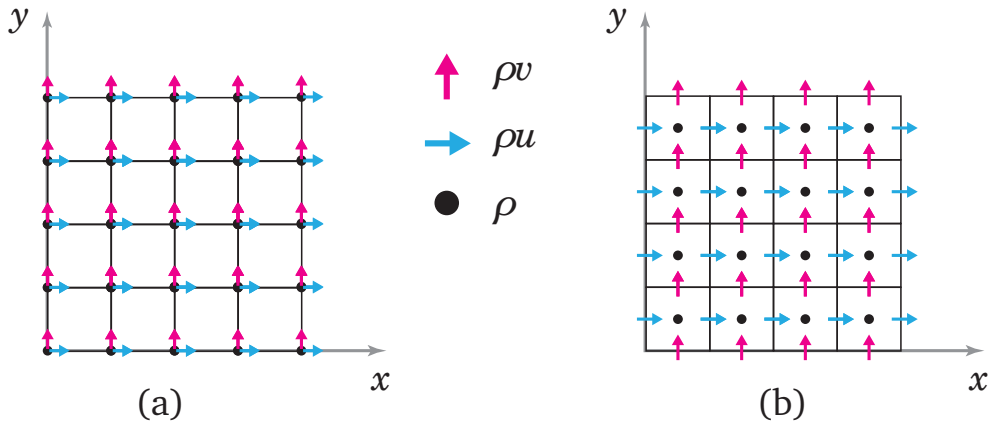

Figure 3.5: Different grid styles used in numerical studies. a) Collocated grid b) Staggered grid.

The Runge-Kutta time-stepping [31] is given as follows:

$$\frac{dy}{dt} = f(y,t), \tag{3.4}$$

from t^n to t^{n+1} using:

$$y^{n+1/3} = y^n + \frac{8}{15}\Delta t f(y^n, t^n), \tag{3.5}$$

$$y^{n+2/3} = y^n + \frac{1}{4}\Delta t f(y^n, t^n) + \frac{5}{12}\Delta t f(y^{n+1/3}, t^{n+1/3}), \tag{3.6}$$

$$y^{n+1/3} = y^n + \frac{1}{4}\Delta t f(y^n, t^n) + \frac{3}{4}\Delta t f(y^{n+2/3}, t^{n+2/3}). \tag{3.7}$$

with the change in time given as : $t^{n+1/3} = t^n + 8/15\Delta t; \qquad t^{n+2/3} = t^n + 2/3\Delta t$

The DNS code has time step determined from the frequency of perturbation of the suction and blowing given as:

$$\Delta t = \frac{2\pi}{\omega}\frac{1}{LP}. \tag{3.8}$$

With the frequency itself calculated as follows:

$$\omega = FMa_\infty \mathrm{Re}_\infty, \qquad \text{with} \quad F = 2\pi f^*(\mu^*/\rho^* u^{*2})_\infty.$$

The 2D modes are calculated for the dimensionless spanwise wave number (B) set as zero.

In the computation domain, The base flow is prescribed at the inlet, while at the wall, a no-slip boundary condition is applied with an adiabatic boundary condition. Close to the outflow and at the top of the computation domain, the solution is damped in the sponge region towards the laminar base flow solution (figure 2.5). Perturbations of a fixed frequency are forced via blowing and suction at the wall at a certain streamwise coordinate x such that $x_s < x < x_e$. The prescribed perturbation is:

$$(\rho v)_{wall} = A_v \sin(\omega t) k \; g(\xi). \tag{3.9}$$

In the above equation $k = 0$ for all $x \notin x_s < x < x_e$, $k = 1$ for $x_s < x < x_{c,strip}$ and k = -1 for $x_{c,strip} < x < x_e$, with $x_{c,strip}$ defined as the midpoint within the disturbance strip. The magnitude of the perturbation $A_v = 0.001 Ma_\infty$, $g(\xi)$ is the shape function given as:

$$g(\xi) = 15.1875\xi^5 - 35.4375\xi^4 + 20.25\xi^3. \tag{3.10}$$

Equation (3.10) uses the auxiliary coordinate ξ to calculate the shape function. The auxiliary coordinate for $x_s < x < x_{c,strip}$ is defined as:

$$\xi = \frac{(x - x_s)}{(x_{c,strip} - x_s)},$$
$$\text{with, } x_s = x_{c,strip} - \frac{L_{strip}}{2}$$

and for $x_{c,strip} < x < x_e$ it is defined as:

$$\xi = \frac{(x_e - x)}{(x_e - x_{c,strip})}$$
$$\text{with, } x_e = x_{c,strip} + \frac{L_{strip}}{2}.$$

The solutions from the `FORTRAN` code at every location is saved into a binary file with a `plot3d` format for easy post-processing and to facilitate viewing the solution on a software such as `tecplot 360`.

3.3.1 Post-processing

The simulations are allowed to run for 600,000 iterations to achieve a steady state, where the sub-harmonics have a reduced amplitude, to be an order-of-magnitude lower than that of the fundamental. In the steady-state conditions, any numerically induced disturbances, if any, would have advected out of the computed domain downstream. Once steady state has been reached, the solution files stored are analysed in Fourier space. For this purpose, a Fourier transform in time and spanwise direction with a fundamental circular frequency $\Omega = \omega/2$ is chosen.

50 solution files are stored within 2 periods of the forcing applied. For a sampling index (l) and discrete time $t_l = 2/50LPl$, The amplification rate based on the streamwise velocity and phase velocity based on wall normal velocity are calculated using:

$$\alpha_i(x) = \frac{1}{\hat{v}_1^{max}} \frac{\partial \hat{v}_1^{max}}{\partial x}. \tag{3.11}$$

3.4 Flow conditions

The *behaviour of any fluid* is characterised by studying the variation of its thermodynamic properties and understanding different regions of importance in diagrams, such as pressure-volume $P-v$ diagram or temperature-entropy $T-s$ diagram. *The flow*, however, is characterised by the variation of both thermodynamic and transport properties in a given environment. This section presents important information about the behaviour of toluene as a fluid and the operating conditions of the fluid.

Figure 3.6a, plots the $T-s$ diagram for toluene. The figure shows the two-phase region, along with isobars ranging from 1 bar to 45 bar. The reference condition for toluene, is clearly indicated and has a freestream temperature T^*_∞ of 450 K, pressure P^*_∞ of 1.8 bar and a Mach number Ma_∞ close to 3. The conditions for critical point are $T^*_c = 591.75$ K, $P^*_c = 41.2630$ bar. Close to the vapour saturation line both the effects of compressibility factor (Z) and the fundamental derivative of gas dynamics (Γ) are important. As mentioned in section 2.3, Γ **characterises the dense gas effects** acting on the fluid while Z **is a measure of deviation of a particular fluid from ideal gas like behaviour**. **Both** Z **and** Γ **together characterise the non-ideal behaviour of toluene.**

Figure 3.6b, plots the contours of Z on a $T-s$ diagram along with the saturation curves. It is observed that contours of $Z < 1$ are close to the critical point, with the lowest value of Z around the critical point (•). The contours of Z form a closed loop spanning the liquid saturation line to the vapour saturation curve around the critical point in a 'bunny-ear' shape. The tip of the bunny-ears for contour lines $Z = 0.75$ and $Z = 0.98$ are not visible in the figure due to the unavailability of data beyond T = 700 K in `Fluidprop`. The reference state ($\star$) is present between the contour lines of $Z = 0.98$ and $Z = 0.75$. Hence, compressibility effects are present in the flow.

Similarly, figure 3.6c plots the contours of Γ on a $T-s$ diagram. The contour lines for Γ also have a bunny-ear shape but are sharper in comparison with the profiles of Z and seem to originate from the critical point and end at the vapour saturation line. The reference state is present within the contour lines of $\Gamma = 0.9$ and $\Gamma = 1$. This means that the fluid in the freestream has dense gas effects. The value of Γ is only an indicative of probable behaviour of the fluid i.e. $\Gamma <$ **1 is not a strong criteria** to determine the behaviour of the fluid. Figure 3.6d shows the variation of Γ along the isobar of 1.8 bar for temperatures varying from 350 K to 700 K. From the figure, it is observed that Γ **is lower than unity until T** $\approx$ **480 K**. The combined contribution of Z and Γ determine the behaviour of the fluid and the variation of its properties along the flow domain.

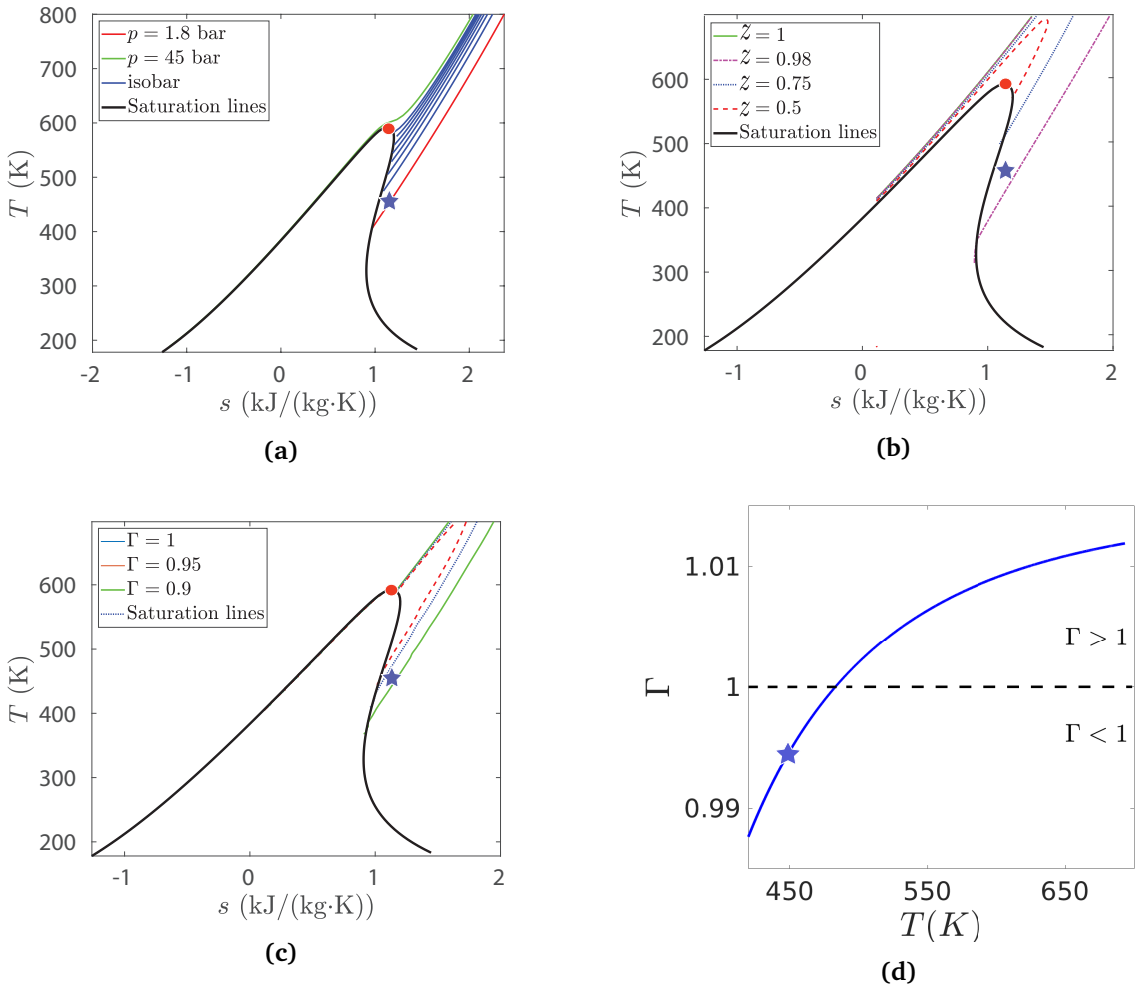

Figure 3.6: (a) $T-s$ diagram for toluene with isobars of pressure; (b) $T-s$ diagram for toluene with contour lines of compressibility factor Z.; (c)$T-s$ diagram for toluene with contour lines of fundamental derivative of gas dynamics Γ; (d)Variation of the fundamental derivative of gas dynamics along the isobar 1.8 bar for toluene. The reference state ⋆ and the critical point • are indicated in the graph.

Chapter 4

Results & discussion

Two gases representing the flow of toluene and an ideal gas, based on the properties of air, are considered in all of the results presented henceforth. The chapter presents the results of the base flow explaining its essential features by comparing the 2 gases. Further, the results of LST performed are explained and the solutions for both the ideal air are toluene flows are contrasted with each other. Finally, the results of the DNS performed for toluene cases are presented and compared with the results from LST.

4.1 Simulation conditions

The procedure adopted in performing each simulation can be broken down to individual steps as explained before (section 2.4). To enhance the readability of the results it is mentioned again. It involves varying the relevant free-stream conditions to match the simulation case, accurately calculating the base flow of the case and then using the base flow as an input for LST solver. The base flow is also pre-processed and then given as an input to the DNS solver. The features of the fluid at free-stream conditions, important details of the numerical code used as well as the post-processing tools employed are explained in chapter 3. All simulations are solved for a free-stream temperature $T^*_\infty = 450$ K and pressure $P^*_\infty = 1.8$ bar. Furthermore, each simulation case is characterised by the Eckert number of the flow. In the results presented, a total of 6 different Eckert numbers Ec_∞ viz. 0.005, 0.05, 0.1, 0.15, 0.2, 0.45 are used. The most relevant Eckert numbers are mentioned in each section and only its corresponding results are presented within that section.

Table 4.1, gives the free-stream flow properties of both gases, for each value of Ec. It is imperative to note that Eckert number does not affect the values of Prandtl number (Pr), ratio of specific heat (γ) and thermal conductivity which are all a function of the free-stream temperature and pressure. More importantly, the Mach number (Ma) is calculated from the Eckert number using its definitions given in equation (2.9) and (2.10) as:

$$Ma = \frac{\sqrt{Ec \cdot C_p \cdot T}}{c}. \tag{4.1}$$

Table 4.1: Reference values of properties in ideal air and toluene flows.

Unit	T^*_∞ K	p^*_∞ bar	Re_∞ -	Pr_∞ -	γ_∞ -	ρ^*_∞ kg/m^3	μ^*_∞ $\times 10^{-5} kg m^{-1} s^{-1}$	$C^*_{p\infty}$ $kJ/kg-K$	κ^*_∞ $J/(m \cdot s \cdot K)$
Ideal gas	450	1.8	10^5	0.72	1.4	4.6236	1.0458	1.673	0.0243
Toluene				0.7442	1.0682			1.7266	

Table 4.2: Mach numbers for ideal air and toluene flows at different Eckert numbers.

Ec	Ma_{ideal}	$Ma_{toluene}$
0.005	0.1118	0.3104
0.05	0.3536	0.988
0.1	0.5	1.3972
0.15	0.6124	1.7112
0.2	0.7071	1.9759
0.45	1.0607	2.9639

Equation (4.1) is used for toluene, but for ideal gas the equation simplifies to give;

$$Ma = \sqrt{\left(\frac{Ec}{\gamma - 1}\right)}. \tag{4.2}$$

The Mach number for both flows are given in table 4.2.

4.2 Base flow

Self-similar solutions are constant pressure flows with varying thermodynamic and transport properties, governed by the system of ODE given in equation (2.25). The flows are solved for Eckert numbers 0.005, 0.05, 0.1, 0.15, 0.2. The Eckert number indirectly fixes the Mach numbers and temperature profiles of the base flow. Figure 4.1, plots the profiles of temperature (subplot (a)), density (subplot (b)), streamwise velocity (subplots (c) and (d)), dynamic viscosity (subplot (e)) and thermal conductivity (subplot (f)) as a function of the wall normal coordinate. Each subplot further contains plots corresponding to flows with an ideal gas (i) and toluene (ii) as fluid.

From figure 4.1, the effect of Ec on both ideal and toluene flows are evident. The effects of Ec are limited to the boundary layer only and the freestream conditions remain unaffected. The influence of the boundary layer spans upto a wall normal coordinate approximately equal to 5 units. The effect of an increasing Ec is the same for both ideal and toluene flows, while the impact of large Ec affects real flows more severely.

Comparing the temperature profiles (subplot (a): (i) and (ii)) it is observed that with an increase in Ec, the temperature in the boundary layer increases attaining its largest value at the wall. The profiles for both ideal and toluene flows are quite similar with no noticeable difference. Thus, the self-similar solution for constant Re and for a fixed fluid is completely determined by Ec. Studying the density profiles for both flows (subplot (b): (i) and (ii)), a decrease in value is observed within the boundary layer reaching a minima at the wall. The decrease in density is more significant at higher Ec. A very minor difference between ideal and non-ideal flows is observed with the value of density at the wall $\rho_w = 4.22\ kg/m^3$ for ideal flow and $4.21\ kg/m^3$ for toluene.

Checking the streamwise velocity profile for both flows (subplot (c): (i) and (ii)), it is observe that increasing Ec shifts the values of u-velocity upwards, i.e. the velocity profile is less fuller at high Ec. This effect is marginal with the increase in the values more for toluene than for ideal gas. This can be noticed more clearly in the zoomed velocity profiles (subplot (d): (i) and (ii)), where the spread in the velocity, i.e. difference between the values of velocity for $Ec = 0.005$ and 0.2 at any particular wall normal coordinate y is more for toluene flows when compared with ideal air flows. For eg. at $y = 2.6$, the velocity profiles have values between 0.74 to 0.77 for ideal air and 0.735-0.77 for toluene.

In contrasting the viscosity profiles for both flows (subplot (e): (i) and (ii)), a significant deviation between the profiles for toluene and ideal air are observed. The difference in profiles are **largest for the thermal conductivity profiles** (subplot (f): (i) and (ii)).

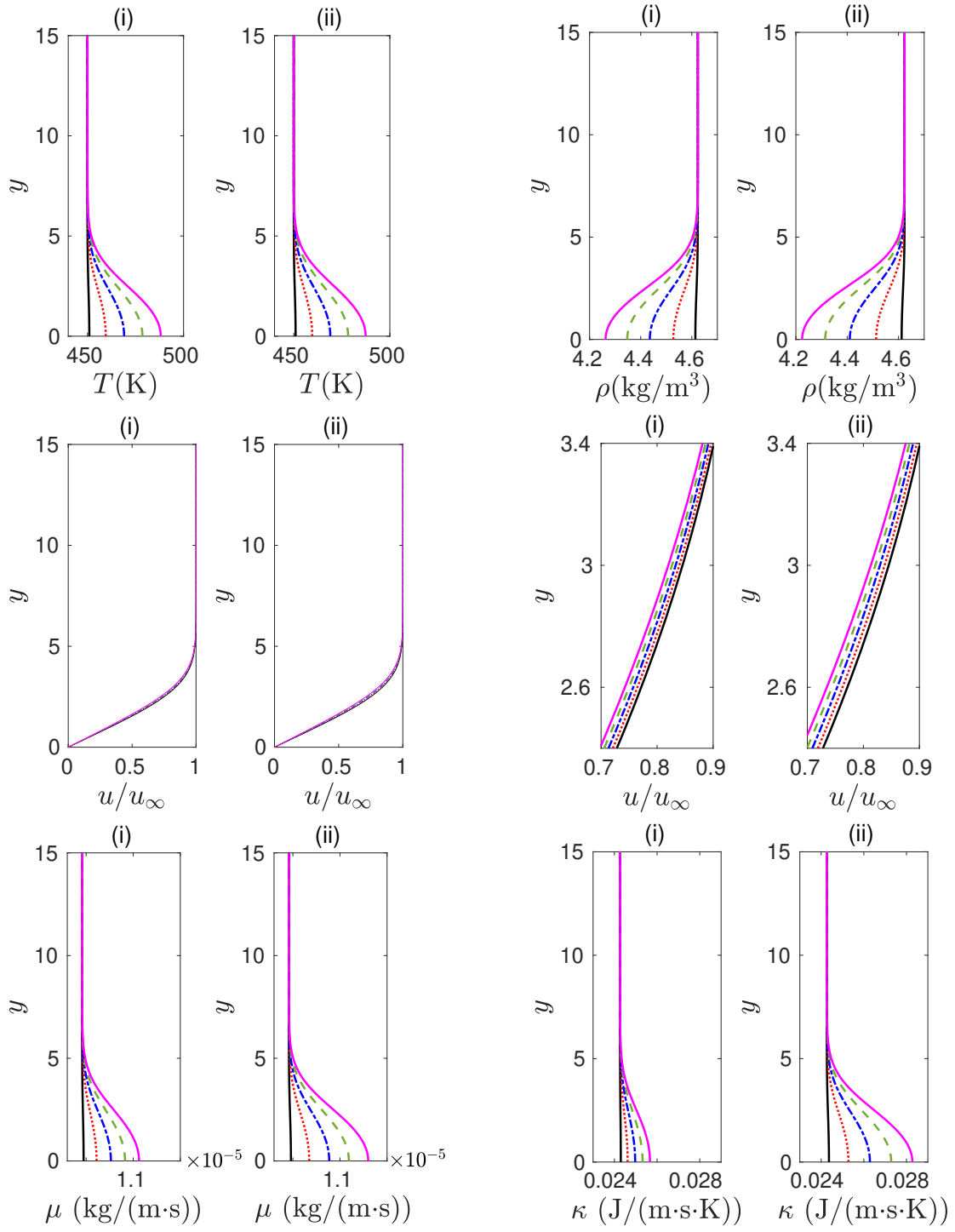

Figure 4.1: a) Temperature profile ($y-T$); b) Density profile ($y-\rho$); c) Velocity profile ($y-u/u_\infty$); d) Zoomed velocity profile($y-u/u_\infty$); e) Dynamic viscosity profile ($y-\mu$); f) Thermal conductivity profiles ($y-\kappa$). Base flow profiles of ideal air flow (i) and toluene flow (ii) for Eckert numbers $Ec = 0.005$ (——), 0.05 (·····), 0.1 (-·-·), 0.15 (- - -) and 0.2 (——).

4.2.1 Discussion

The base flow profiles generated are similar to the self-similar solution obtained by Prandtl and Blasius. Furthermore, for all thermodynamic and transport properties, the influence of the boundary layer increases as Ec increases. A high value of Ec signifies a larger viscous heating within the boundary layer. Thus, resulting in a larger temperature gradient across the boundary layer. Every other thermodynamic quantity is a function of the temperature. This implies a larger impact for higher values of Ec. This manifests as a decrease in density as temperature increases within the boundary layer and similarly an increase in viscosity and thermal conductivity for an increase in temperature.

The difference in flows of toluene and ideal air manifest mainly in the values of dynamic viscosity and thermal conductivity. This is due to the difference in the way viscosity and thermal conductivity are calculated for both flows. For toluene, viscosity is directly taken from the 1D look-up table whereas for ideal flows the Sutherland law is used to calculate the viscosity. Apart from directly affecting the absolute values of these thermodynamic properties at different regions within the flow, this difference in viscosity and thermal conductivity profiles affects the derivatives and double derivative of these terms, which are later used in solving the stability equation.

The results obtained by self-similar solutions are checked for accuracy by running a DNS and is found to be accurate and robust for both non-ideal and ideal flow.

4.3 LST

The objective of the section is to investigate the performance of linear stability analysis in predicting the behaviour of the flow. The numerical concepts as well as the post-processing are given in section 3.2. The numerical analysis of LST were performed for all Eckert numbers but the results presented in the section are limited to Eckert numbers of 0.005, 0.05, 0.1, 0.15 as these Eckert numbers are sufficient to form a complete narrative on the effect of non-ideal behaviour on the modal stability of the flow.

4.3.1 Eigenvalue spectrum analysis

For ideal gas

For any Eckert number, the eigenspectrum is initially evaluated at $Re_x = 2000$ and $F =$ 10E-6. The solutions are calculated as mentioned in section 3.2. Figure 4.2a, shows the eigenvalue spectrum for an ideal gas at $Ec = 0.005$. The discrete unstable mode (*), fast acoustic modes (mode F) and the entropy-vorticity modes are visible for this Ec. The presence of a strong unstable mode in the 4th quadrant of the α_i-α_r plot is typical to the different results surveyed in the review paper by Federov [8] as well as the theoretical analysis performed by Mack [25]. Fig 4.2b, plots the eigenfunctions of the unstable mode. As explained in section 3.2, the 5 plots have a significant value in the boundary layer i.e. $y < 5$ and in the freestream, they reduce in magnitude and taper down to zero. Close to the wall, the streamwise velocity u has the largest value and dominates the behaviour of the mode. Farther from the wall, the streamwise velocity is overshadowed by the density ρ. Similarly, the eigenspectrum for $Ec = 0.15$ and the eigenvector of the discrete unstable mode are given in figure 4.3. The results in figure 4.3 are similar to that obtained for $Ec = 0.005$. No important difference in the results implies that the effect of Ec on ideal flows are weak.

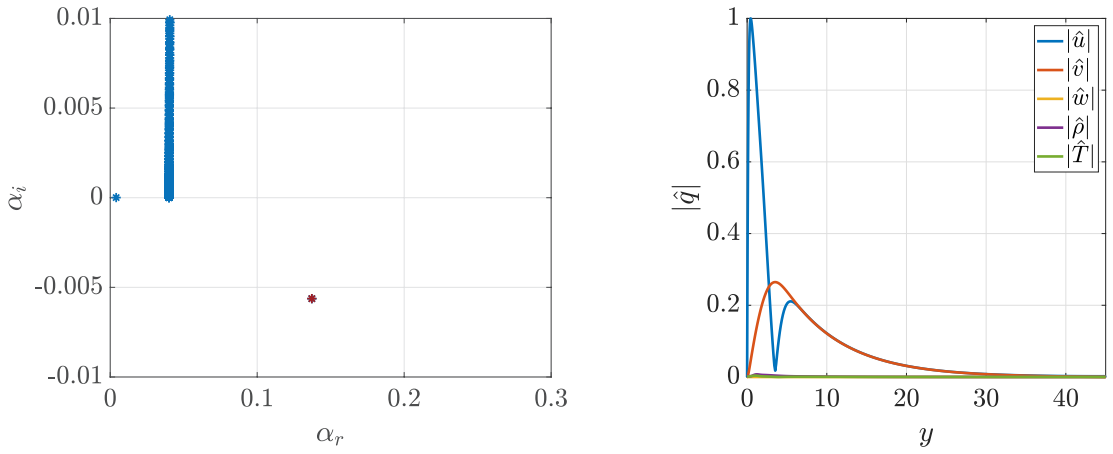

(a) **(b)**

Figure 4.2: (a) Eigenvalue spectrum indicating the unstable mode (*); (b) Eigenfunction of the unstable mode. Corresponding plots for ideal air flows at $Ec = 0.005$.

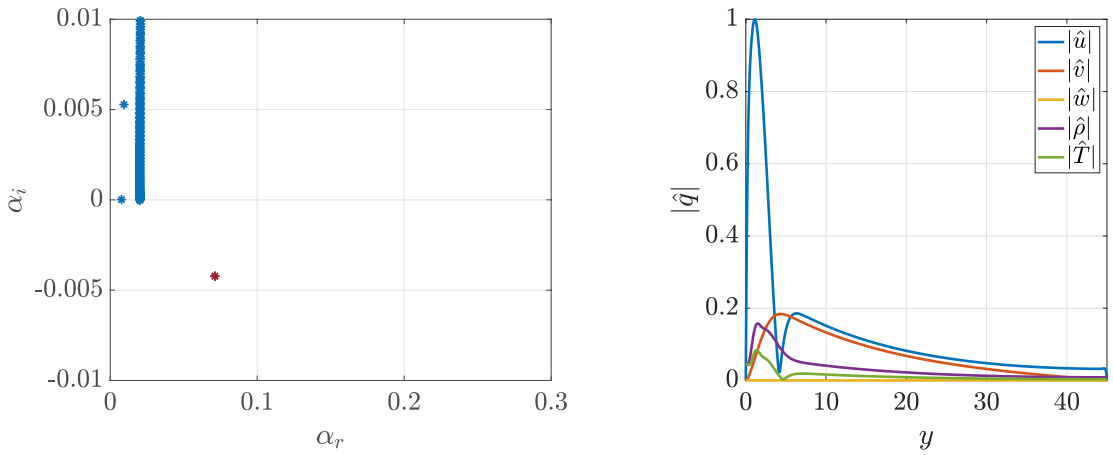

(a) **(b)**

Figure 4.3: (a) Eigenvalue spectrum indicating the unstable mode (*); (b) Eigenfunction of the unstable mode. Corresponding plots for ideal air flows at $Ec = 0.15$.

For toluene

Similar to the analysis performed for ideal gas, the LST for toluene are carried out for a local Reynolds number $Re_x = 2000$ and dimensionless frequency of $F = 10\text{e-}6$. The eigenvalue spectrum and the corresponding eigenfunctions for $Ec = 0.05$ are plotted in figure 4.4. The distribution of eigenmodes in the eigenvalue spectrum as well as the variation of the profiles in the eigenfunction plot are similar to the results of ideal air.

Figure 4.5a, shows the eigenvalue distribution for $Ec = 0.15$. Unlike the previous cases the modes can be observed to be more densely packed. The discrete unstable mode is no longer present and the continuous spectrum of mode S is visible. The 2nd mode beyond the entropy/vorticity modes appears to lie within the 4th quadrant of the figure (indicated in *). An increase in Re_x to 4000 results in figure 4.6b. It is observed that at $Re_x = 4000$, modes 3-6 are all within the 4th quadrant and fall under the unstable criterion (highlighted in red).

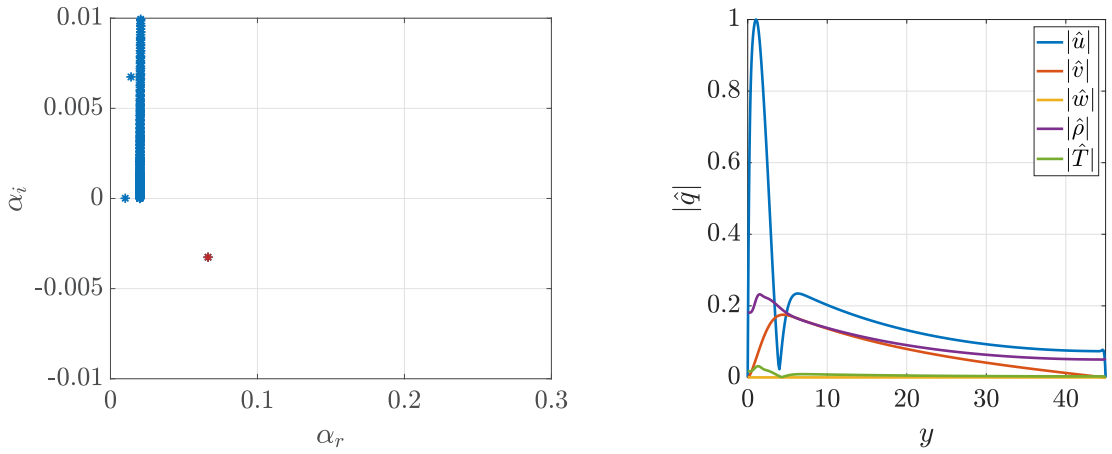

(a) **(b)**

Figure 4.4: (a) Eigenvalue spectrum indicating the unstable mode (*); (b) Eigenfunction of the unstable mode. Corresponding plots for toluene flows at $Ec = 0.05$.

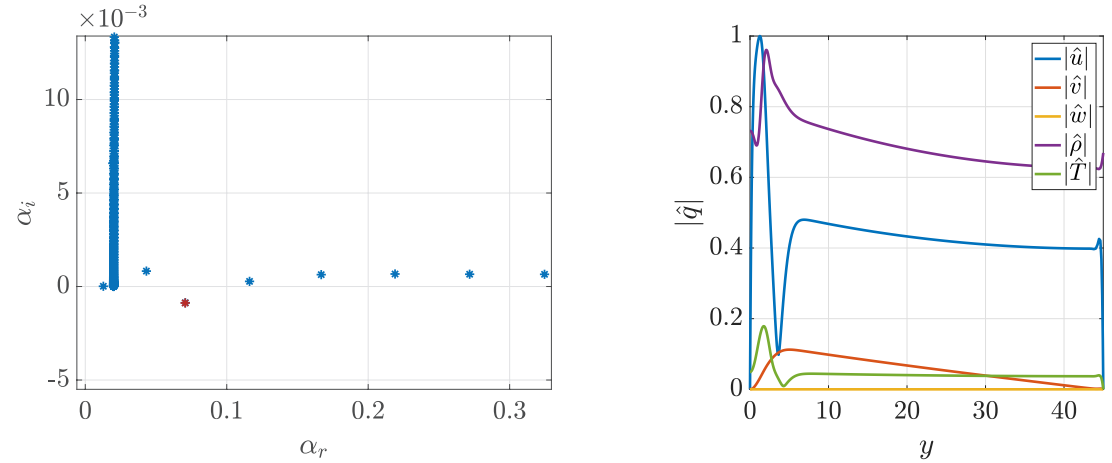

(a) **(b)**

Figure 4.5: (a) Eigenvalue spectrum; (b)eigenfunction. Profiles of the unstable mode for flows of toluene with $Ec = 0.15$.

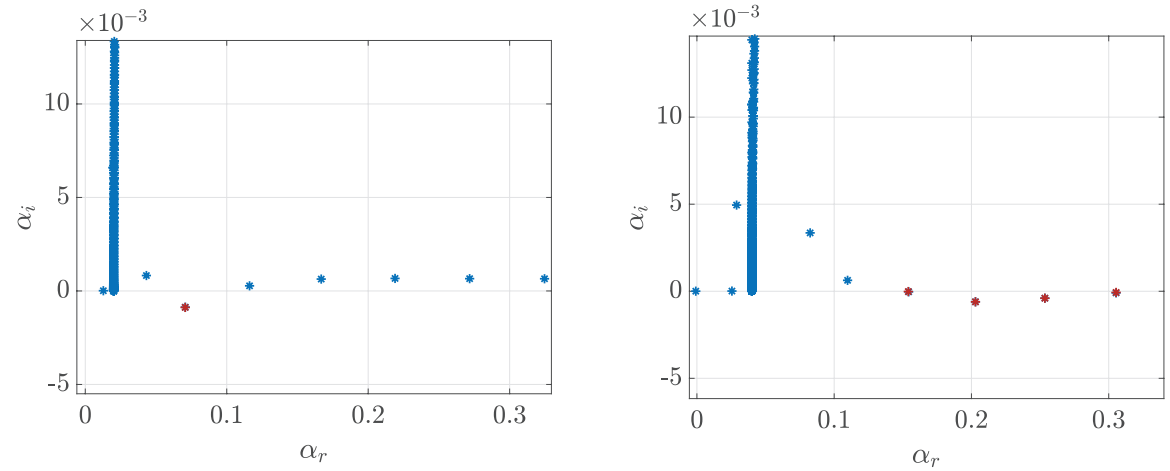

(a) **(b)**

Figure 4.6: (a) Eigenvalue spectrum evaluated at $Re_x = 2000$; (b) Eigenvalue spectrum evaluated at $Re_x = 4000$. Eigenvalue spectrum of the solutions to the stability equations at different initial values. The unstable mode(s) are highlighted in *.

By inspecting the corresponding eigenvectors of the first 6 modes in the mode S spectrum in figure 4.7, we observe that mode 1 is the closest to the boundary layer like eigenvector profiles. From mode 2 onwards, each mode has a presence of wave-like fluctuations within the profiles of every single quantity. Moreover, the profiles of each of the eigenfunction has a non-zero value in the freestream suggesting a non-physical behaviour. It is also observed that the number of waves present within the y-computation domain increases linearly for each subsequent modes similar to modes of higher harmonics or acoustic modes.

To check for the presence of numerical modes, the stability analysis is repeated at $Re_x = 2000$ for a different grid with the domain in the wall-normal direction doubled ($y_{max} \rightarrow 90$). The results of the 2nd grid eigenvalue spectrum (∘) are plotted on top of the results of grid 1 (*) as shown in figure 4.8.

In the figure, it is clearly observed that the two markers corresponding to the different grids do not match perfectly. The entropy/vorticity modes match qualitatively but the modes in the slow and fast acoustic mode are offset for the two grids except for mode 1. Thus, it can be inferred that the acoustic modes that lie in the unstable region of the eigenvalue spectrum are numerical and non-physical and the physical mode (mode 1) is stable. Therefore, there are **no unstable modes at $Ec = 0.15$**

4.3.2 Stability diagrams

For ideal gas

For each LST simulation, the most unstable mode is tracked for Re_x ranging from 0 to 2000 and F ranging from 0 to 250e-6. Figure 4.9, plots the neutral curve profile as explained in section 3.2 for different Ec. The figure consists of 4 plots in a mirrored coordinate system of dimensionless frequency F and local Reynolds number Re_x. The figure shows the distribution of the local growth rate (α_i). In each of the four plots, the contours are plotted for growth rate from zero, corresponding to the neutral curve and upwards to more unstable regions within the neutral curve. The neutral curve for $Ec = 0.005$ are plotted on every other stability diagram plot with dotted lines for better visualisation of the changes in the unstable region. From the plots, it is evident that with an increase in Eckert (Mach) number, the growth rate reduces and the neutral curve shrinks and hence stabilises the flow.

Another important property from LST is the phase velocity of the perturbation (c). Figure 4.10, plots the phase velocity as a function of F and Re_x. The figure is also split into 4 plots with a mirrored coordinate system, with each plot corresponding to a particular value of Ec. In each plot, the corresponding neutral curve is plotted in solid black lines to give a visual representation of the phase velocity of the perturbation in the unstable region. From the figure, it is observed that the phase velocity of the unstable region is between 0.3-0.4 and does not change significantly for an increase in Ec.

For toluene

Similar to the analysis of ideal flows, stability diagrams in mirrored coordinate systems for growth rate and phase velocities are also plotted for different Ec. Figure 4.11 shows the growth rate of the perturbations for different Ec. The effect of dense gas and non-ideal effects for toluene are very prominent in this image. The neutral curve at $Ec = 0.005$ for toluene is very similar to the neutral curve of ideal flow, but as Ec increases the size of the unstable region reduces drastically with a severe reduction in the magnitude of the growth rate at the centre of the unstable region. At $Ec = 0.10$, the neutral curve is weak and the unstable region is minuscule and **at $Ec = 0.15$, no neutral curve is observed**. This suggests the *presence of no growing mode for flows with $Ec > 0.15$* similar to the observations made in the eigenvalue spectrum analysis.

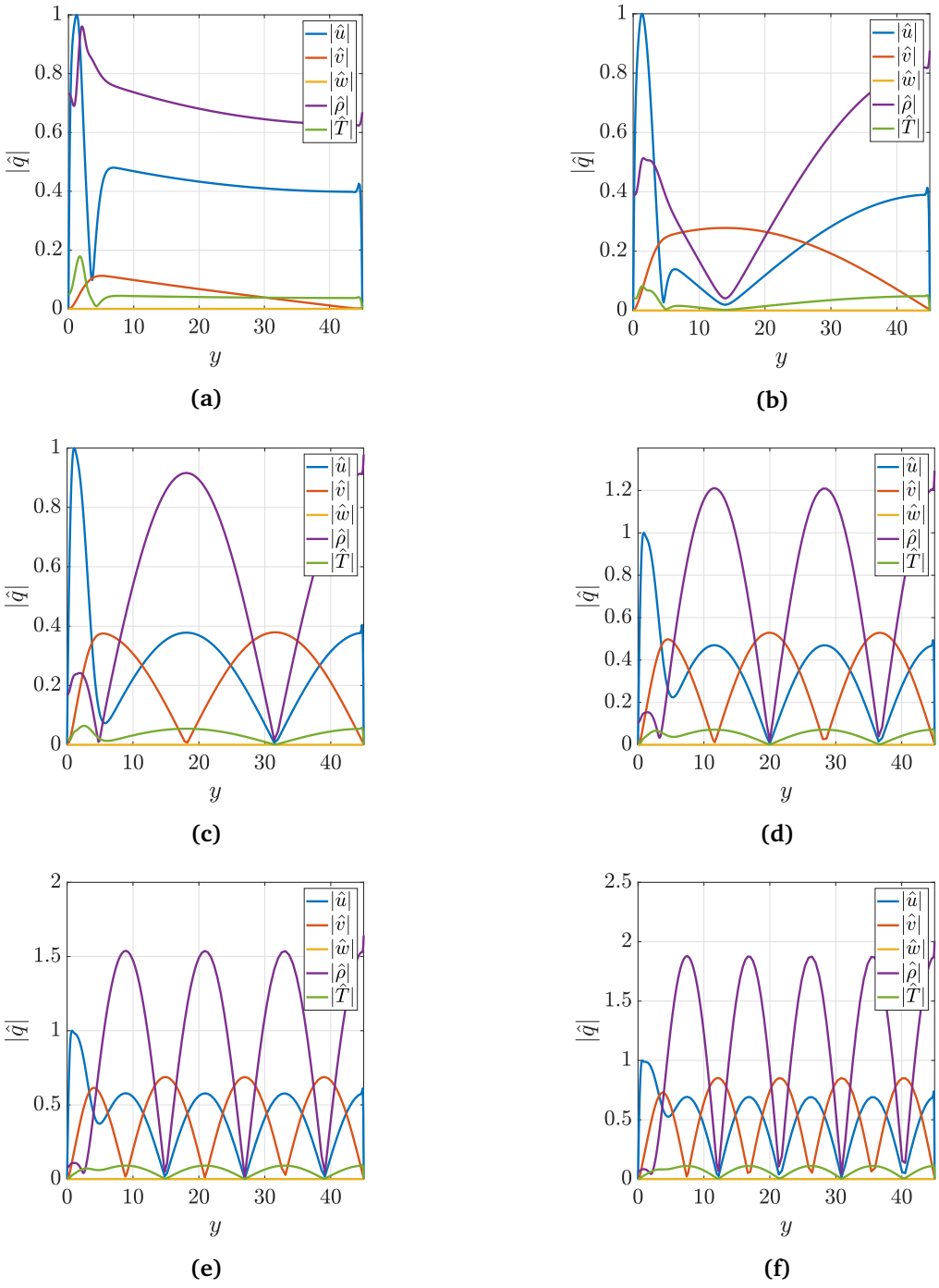

Figure 4.7: (a) mode 1; (b) mode 2 ; (c) mode 3; (d) mode 4; (e) mode 5; (f) mode 6. Eigenfunctions of each mode corresponding to the eigenvalue spectrum in figure 4.5.

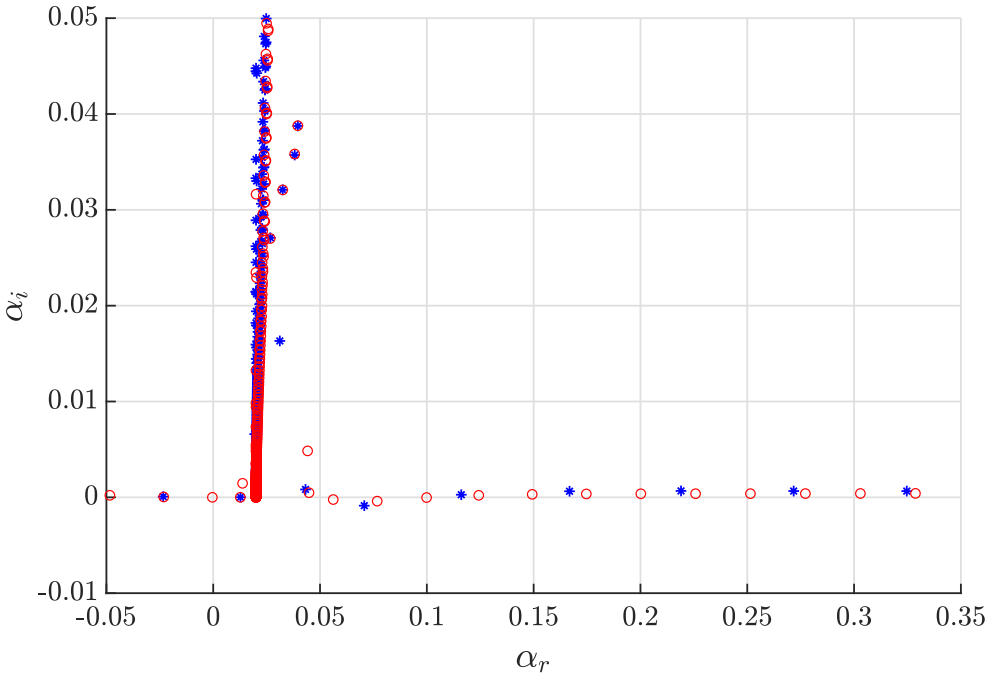

Figure 4.8: Eigenvalue spectrum for $Ec = 0.15$ at $Re_x = 2000$ for grid 1 * with $y_{max} = 45$ and grid 2 ∘ with $y_{max} = 90$

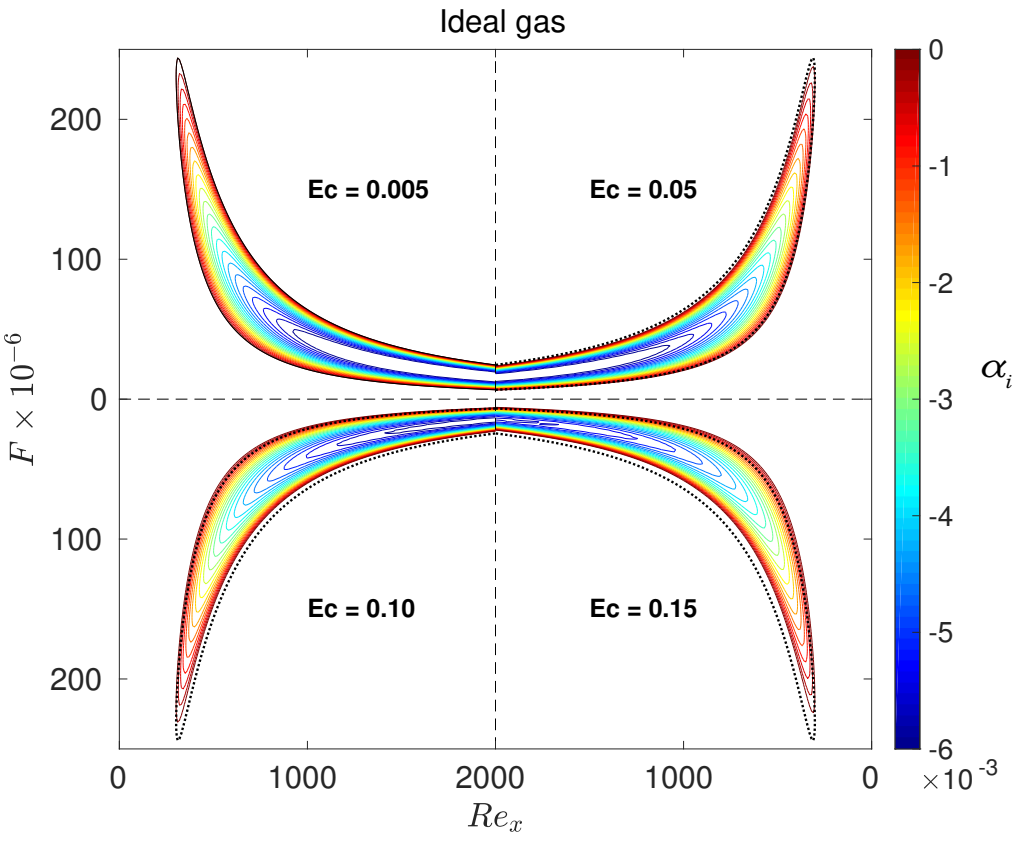

Figure 4.9: Growth rates of the perturbation in the $F - Re_x$ stability diagram for ideal air.

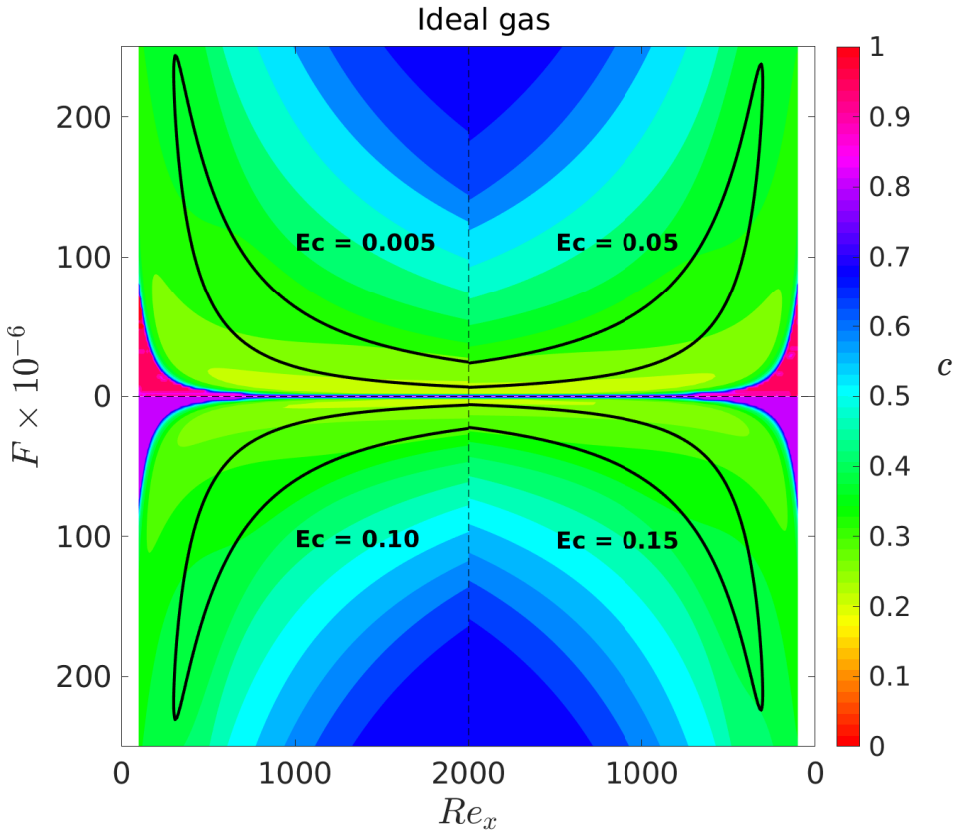

Figure 4.10: Phase velocity of the perturbation in the $F - Re_x$ stability diagram for ideal air.

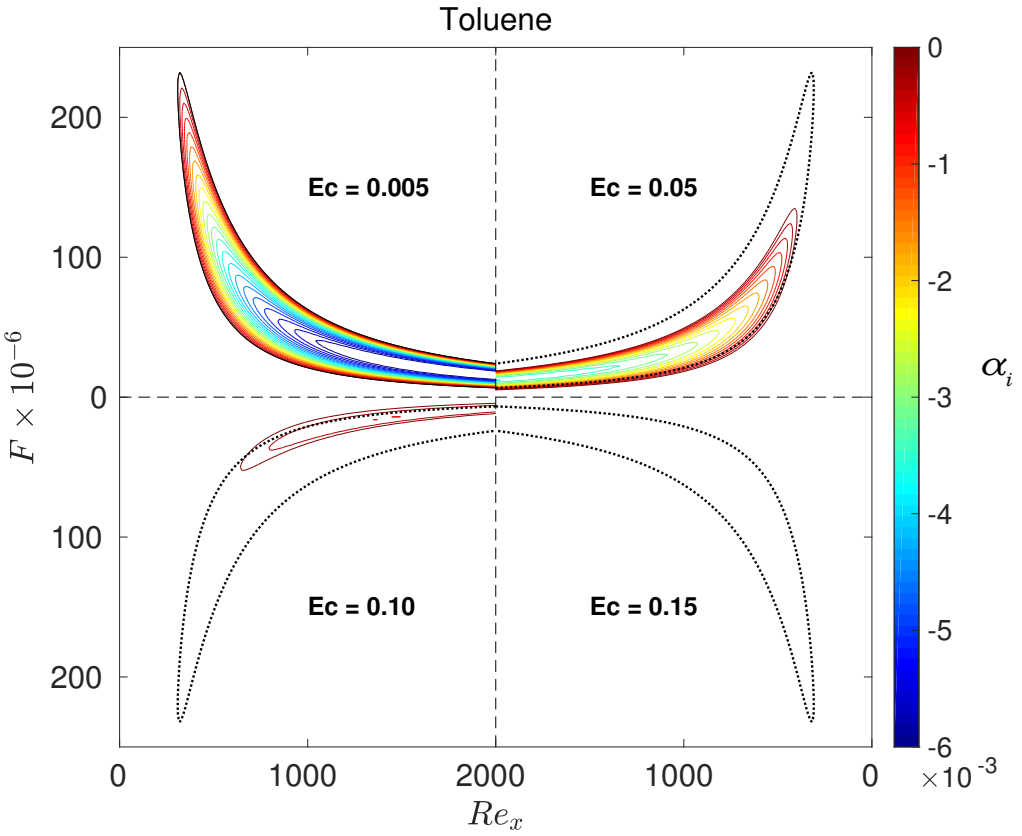

Figure 4.11: Growth rates of the perturbation in the $F - Re_x$ stability diagram for toluene.

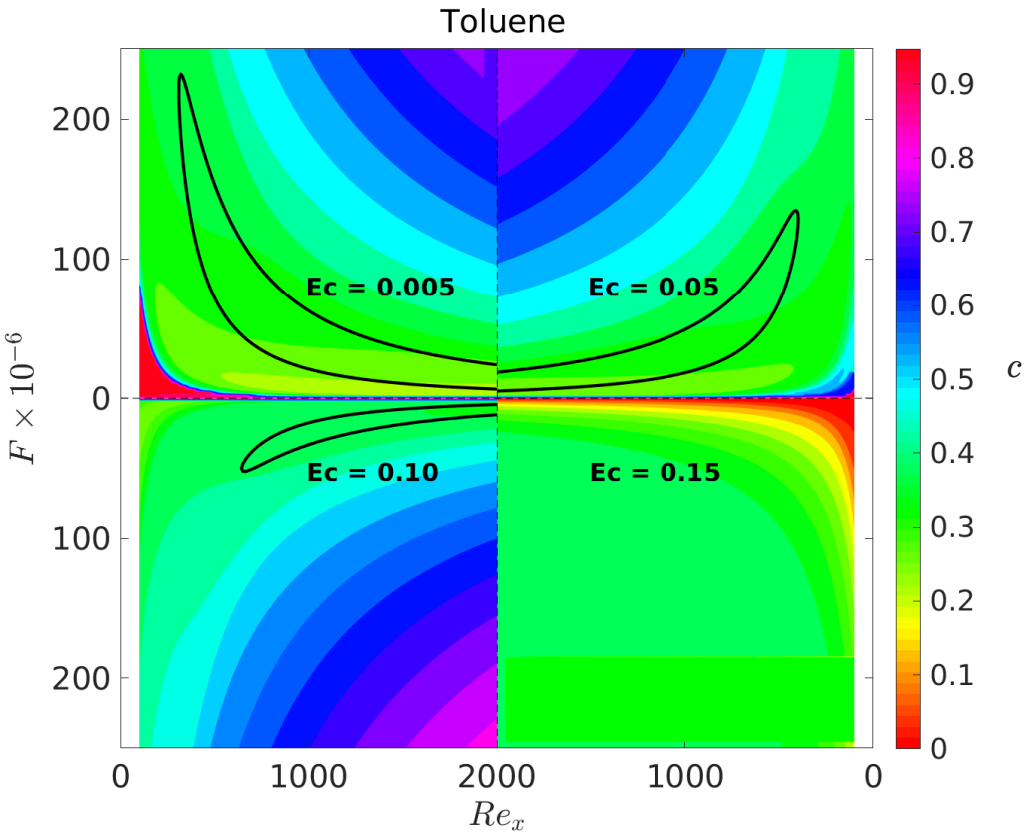

Figure 4.12: Phase velocity of the perturbation in the $F - Re_x$ stability diagram for toluene.

Figure 4.12, plots the variation of phase velocities with the corresponding neutral curve regions. It is noticed that, the phase velocity within the neutral curve is 0.2-0.4 and the values of the phase velocity do not change significantly for an increase in Ec. Furthermore, for $Ec = 0.15$, the regions with a high value of F show no contours of phase velocity and remains relatively unchanged throughout the plot. The unique results can be attributed to the fact that LST predicts no unstable mode and the behaviour of the tracked mode is not correct for all F.

4.3.3 Discussion

Figure 4.11, shows a strong stabilising effect of Ec. For a more detailed understanding, neutral curves are plotted for every 0.1 increment in Ec, given in figure 4.13. In the figure, the neutral curve of $Ec = 0.05$ are plotted as dotted lines in all subsequent plots for better visualisation in the change in the neutral curve. It is observed that for every increment in Ec there is a steady decrease in the size and intensity of the neutral curve. Beyond $Ec = 0.12$, there is no neutral curve and the flow has no growing eigenmode **predicting the flow to be modally stable for all $Ec > 0.12$**.

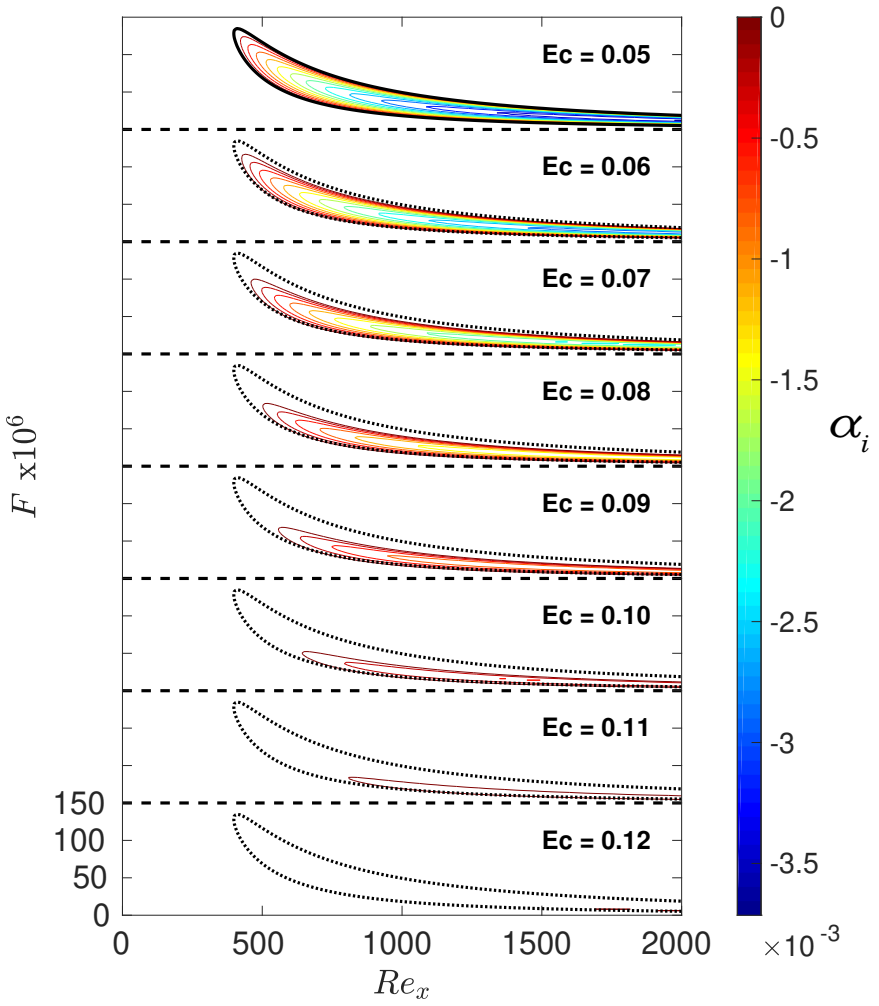

Figure 4.13: Growth rates of the perturbation in the $F - Re_x$ stability diagram for toluene for Ec ranging from 0.05 to 0.12.

The above research considers only the spatial problem for a 2D perturbation. To analyse the effect of oblique modes on the neutral curves, the stability analysis are performed for increasing values of the non dimensional spanwise wavenumber B. Figure 4.14a, is a 3D contour plot with the neutral curve generated plotted in higher planes corresponding to a higher spanwise wave number B. The Neutral curve of each plane are represented in a single 2D plot in figure 4.14b. From both figures, it is visible that increasing B at $Ec = 0.05$ reduces the size and intensity of the unstable region implying that the 2D disturbances are the primary contributor to modal instability.

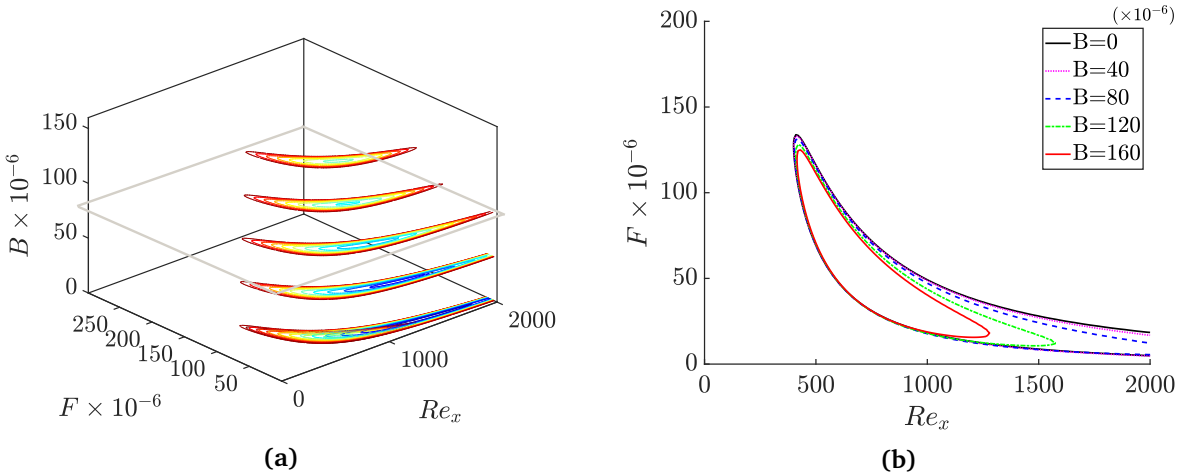

Figure 4.14: a) 3D contour plot of the neutral curve for different values of local Reynolds number Re_x, dimensionless frequency F and spanwise wavenumber B; (b) Representation of subplot (a) on a 2D plane.

4.4 DNS

In order to account for the shortcoming of LST such as the non-parallel base flow, DNS is performed for 4 Eckert numbers viz. 0.05, 0.1, 0.15 and 0.45. The domain of the DNS is chosen in accordance with the results obtained from LST. Figure 4.15, shows the DNS domain chosen for $Ec = 0.05$ and 0.1. The DNS domain remains unaltered for $Ec = 0.15$ and 0.45.

In each DNS simulation, the x-domain ranges from $x_0 = 1$ upto $x_1 = 45$. It is important to note that a local Reynolds number $Re_x = 2000$ corresponds to an $x = 40$. Thus, the domain of DNS is larger than the LST results (illustrated by dashed lines) to prevent any effects due to the sponge region. The sinusoidal perturbations given in equation (3.9), are introduced at $x = 4$. The perturbations have a fixed $F = 30$e-6 and an amplitude of $O(10^{-4})$, ensuring the perturbations remain in the linear regime.

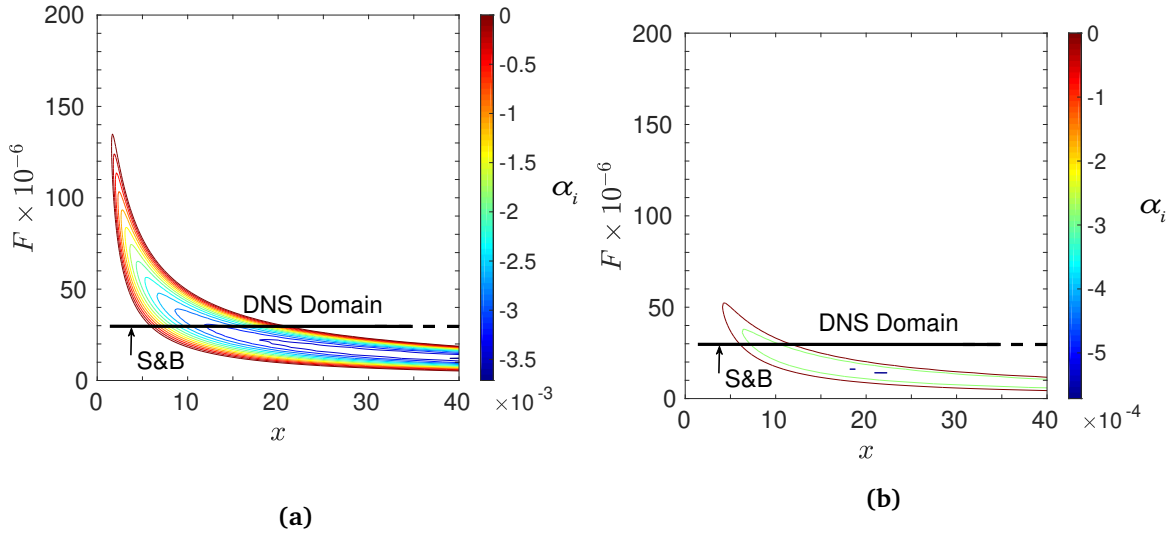

Figure 4.15: (a) $Ec = 0.05$; (b) $Ec = 0.10$. Representation of the DNS domain used for different simulation cases.

As shown in figure 4.15, the DNS frequency F is chosen such that it pierces through the unstable region, capturing the entire region where modal growth is expected to occur. Each simulations is allowed to achieve steady state before the solutions are stored.

Figure 4.16, shows a typical perturbation profile of wall normal velocity for a DNS simulation. The perturbation profile has 4 separate regions of importance. For x upto 4 the behaviour of the flow is laminar (region-1) and closely resembles the base flow. Beyond $x = 4$, the flow enters the receptive region (region-2) where the forced perturbations enter the flow and excite the free or natural modes. The flow exits the receptive region at $x = 7$. The flow is within the neutral curve, where the modal growth of the perturbations occur and the disturbances grow in magnitude (region-3). Beyond $x = 22$, the flow exits the unstable region and the decaying modes result in the reduction in amplitude to return back to a laminar flow. It is key to note that **in the freestream the flow always decays the perturbations** and the **perturbation profiles follow the results of LST only in regions 3 and 4**.

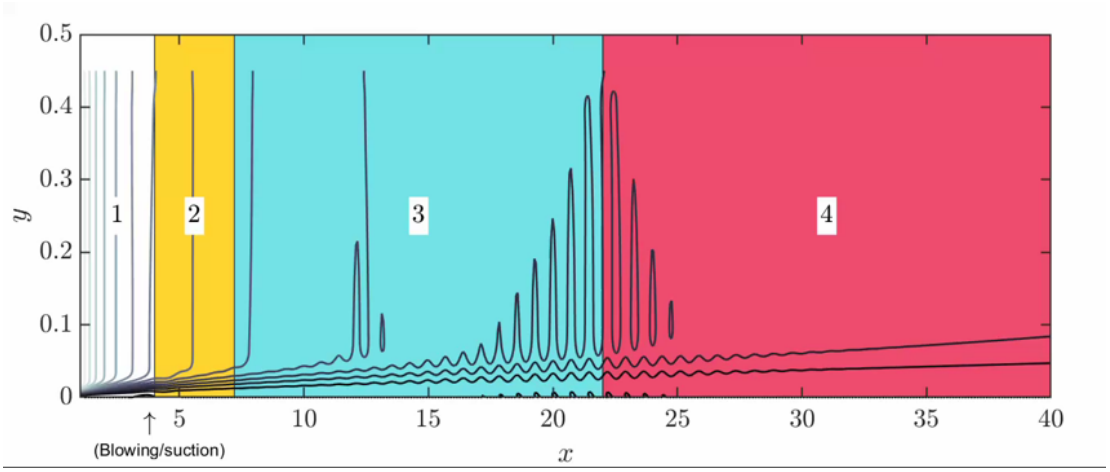

Figure 4.16: Contour of perturbations in wall normal velocity obtained from DNS results for $Ec = 0.05$. Figure shows region of laminar flow (1), receptive stage (2), modal growth within the unstable region (3) and modal decay after the unstable region (4).

The results for each Eckert number is quantitatively represented in figure 4.17. The figure plots the growth rate (4.17 (a), (c) and (e)) as well as the phase velocity (4.17 (b), (d) and (f)) of the perturbation as a function of the streamwise coordinate. The plots compare the solutions obtained from LST (—) and DNS (∘). The growth rate and phase velocity for DNS are calculated as mentioned in section 3.3.

The DNS results are plotted using a local average to filter numerical oscillations, with the averaged data points sampled such that the DNS data appears smooth for adequate and clear representation. For all Ec, it is observed that the results from DNS and LST match relatively well.

For $Ec = 0.05$, from figure 4.17 (a), the LST predicts a growth for x between 6 and 22. which is exactly tracked by the DNS results. Furthermore, at high values of x, the results of DNS and LST start diverging. This deviation is present only when the mode is sufficiently stable and is hypothesised to be the contribution of other decaying modes at the same streamwise position. It is important to remember that linear stability results track the role of a single mode in its contribution for growth of perturbations but is not the only significant contributor to their decay. From figure 4.17 (b), we notice that the results of DNS and LST match perfectly. This implies a strong validation for LST in predicting the stability of flows of toluene for low Ec.

Unlike $Ec = 0.05$, for $Ec = 0.10$ the growth rate matches only qualitatively with the results from LST (figure 4.17 (c) and (d)). The growth rate predicted by LST is very small and the DNS is incapable of capturing these small but growing waves accurately and completely. Further, the results at higher x deviate from the predictions made by linear stability, likely due to the superposition of multiple modes. The phase velocity, however, still matches perfectly throughout the DNS domain. The deviation in growth rate are more prominent for $Ec = 0.15$ (figure 4.17 (e) and (f)). More importantly, for $Ec = 0.15$, the results of *DNS also concurs with the predictions from linear stability of a completely*

stable flow for modal growth. This stability in flow could be reason why both, growth rate and phase velocity match only qualitatively, with an offset in value.

Figure 4.17, only compares the post-processed data of growth rate and phase velocity. Figure 4.18 however, plots the variation in the magnitude of perturbation in streamwise velocity ($\hat{u}$), wall normal velocity ($\hat{v}$) and density ($\hat{\rho}$) as a function of a modified wall normal coordinate ($y \cdot Re/Re_x$). A modified wall normal coordinate is necessary as the DNS and LST results have different grid points in the wall normal direction. The eigenfunctions plot at $Ec = 0.05$ (figure 4.18 (a)) are a perfect match between LST and DNS. The comparison for $Ec = 0.1$ (figure 4.18 (b)) are similar to $Ec = 0.05$ and the results of LST and DNS match perfectly with only a slight offset in values for density.

The results for $Ec = 0.15$ however, show a different trend. It is evident from figure 4.18 (c), that the results between DNS and LST only match qualitatively. The streamwise velocity plot of DNS peaks earlier than LST, while the wall normal velocity is over predicted by LST at high $y \cdot Re/Re_x$. It is also observed that the offset in density has increased in magnitude compared to $Ec = 0.10$ case. This behaviour is once again attributed to the stability of the flow and the likelihood of contributions of multiple modes superposition to give the final DNS result.

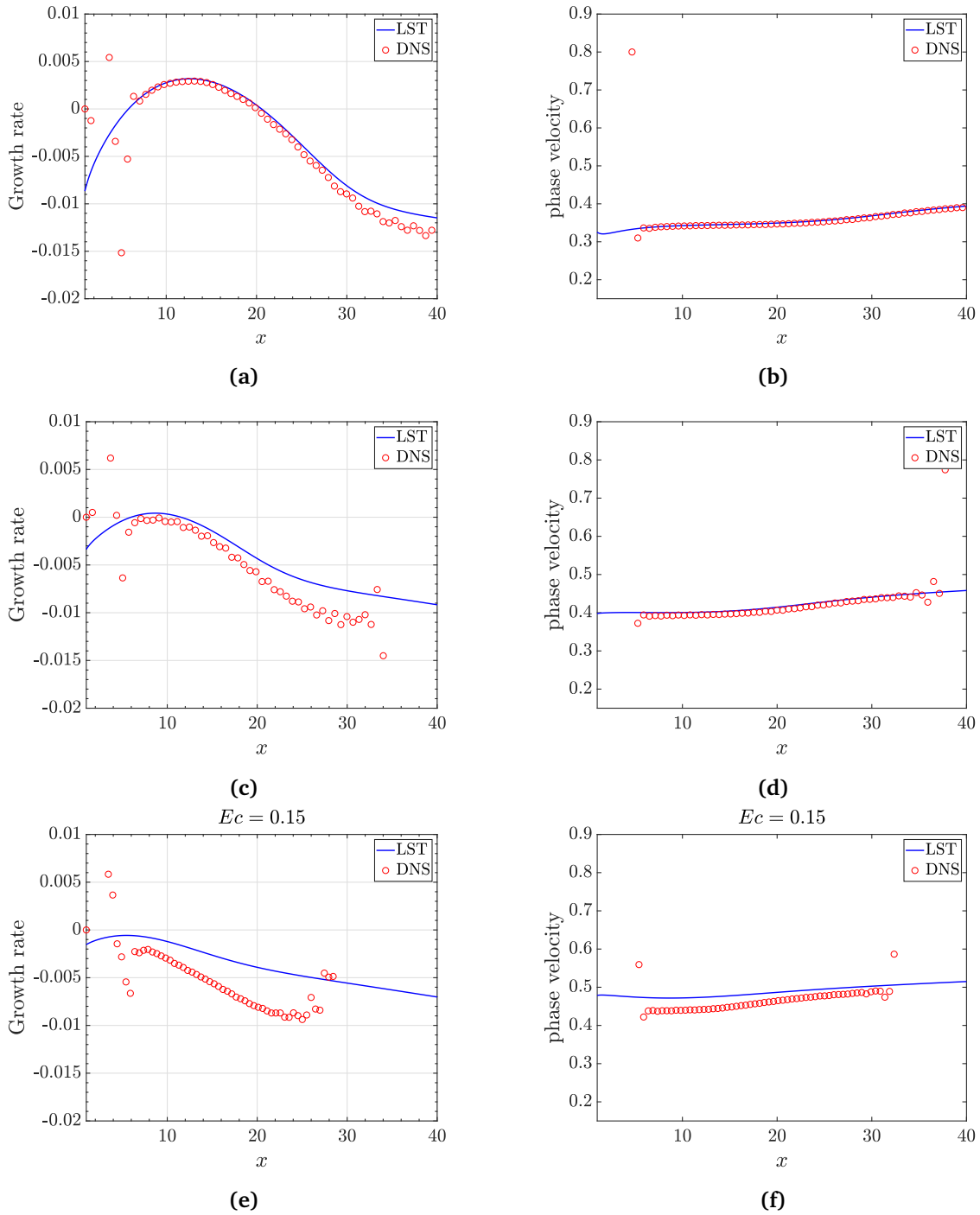

Figure 4.17: (a) Growth rate for $Ec = 0.05$; (b) phase velocity for $Ec = 0.05$; (c) Growth rate for $Ec = 0.10$; (d) phase velocity for $Ec = 0.10$; (e) Growth rate for $Ec = 0.15$; (f) phase velocity for $Ec = 0.15$. Comparison between the results obtained from DNS (∘) and the results predicted by LST (——).

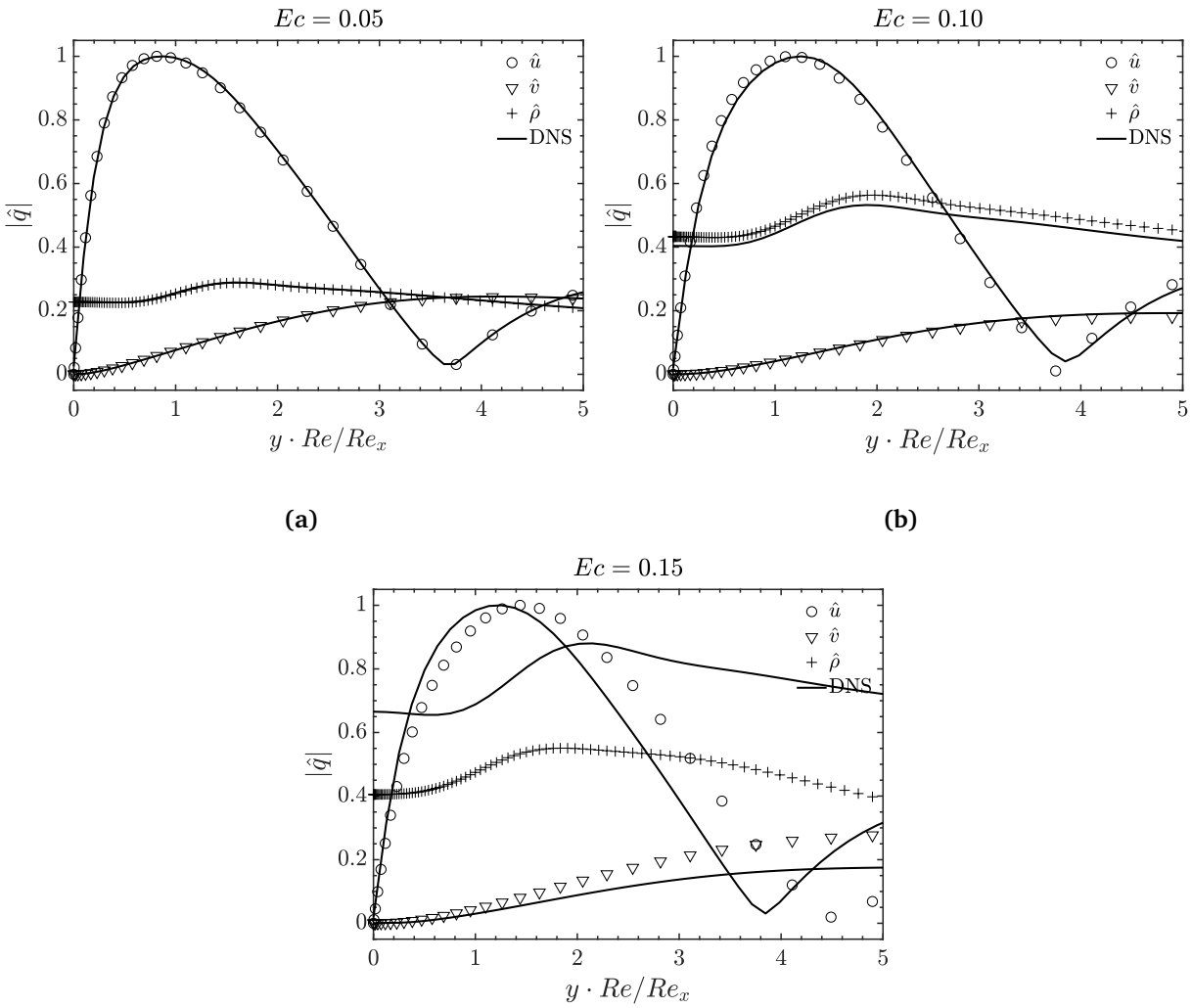

Figure 4.18: (a) Ec =0.05; (b) $Ec = 0.10$; (c) $Ec = 0.15$. Comparison between eigenfunctions from DNS and corresponding plots of magnitude of perturbations in streamwise ($\circ$), wall normal velocity ($\triangledown$) and density (+) as predicted by LST.

4.4.1 Discussion

From the comparison between the DNS and LST results for different Ec, it is clear that both LST and DNS results match with each other qualitatively and quantitatively. This agreement between the 2 results are more evident for growing regions of the flow and the *divergence in results are only in the stable region*. Moreover, it is observed that as Ec increases, the DNS and LST results diverge from each other. This is due to the stabilising effect of increasing Ec on the flows as observed in figure 4.12.

It is also observed that for high values of Ec (> 0.15), the flow is predicted to be completely stable under modal stability from both DNS and LST. Apart from the vanishing of the primary mode of instability, the lack of appearance of secondary modes of instability, observed by Mack for hypersonic flows over a flat plate and for non-ideal flows of CO_2 over a flat plate by Ren et al., indicates the *presence of no unstable modes* for 2D perturbations and from figure 4.14a, we can conclude the flows to be stable for oblique modes as well. This cements the result of **no modal instability for high** Ec **flows over a flat plate for toluene**.

Table 4.3: Values of individual terms in the perturbation energy budget.

	Ec=0.05	Ec=0.10	Ec=0.15
Θ_r	0.0062	0.0018	-0.0068
P_r	0.0089	0.0036	-0.0048
K_r	0.0000	0.0000	0.0000
T_r	-0.0011	0.0001	0.0000
V_r	-0.0016	-0.0019	-0.0020

Perturbation energy budget

Stable flows at supersonic conditions has not been reported for flat plate flows in literature prior to this research. This merits a more fundamental understanding of the growth of perturbations for flows upto $Ec = 0.15$. To fulfill this requirement, a perturbation energy budget analysis is performed on the flow. The perturbation energy equation as well as each term used as well as its significance is explained in appendix B. Table 4.3, depicts the values of each component of the perturbation energy. Here, Θ_r is the most significant term, and it represents the growth in the perturbation energy due to the spatial growth. A positive value of Θ_r signifies a growth in the overall perturbation energy whereas a negative value of signifies a decay of the perturbation energy.

In the table, it is clearly observed that for $Ec = 0.05$ and 0.10, Θ_r is positive. The production term P_r, is the only contributor to the positive value of Θ_r, while the viscous dissipation term V_r is always negative. The negative V_r acts as a dampener and tries to stabilise the flow. More importantly, Θ_r decreases in magnitude as Ec increases from 0.05 to 0.1, with the decrease in Θ_r mainly due to decrease in P_r.

For $Ec = 0.15$, both Θ_r and P_r are negative (in red) while viscous dissipation V_r remains relatively unchanged. The negative value of Θ_r signals a stable flow. **The perturbation energy budget matches with the results predicted by both LST and DNS**. The stability at $Ec = 0.15$ can be attributed to negative value of P across the domain. Figure 4.19, provides more insight in the variation of P for the different values of Ec. The terms contributing to P are split into two terms viz. $\rho_0 \partial u_0 / \partial y$ and -real($\hat{v}\hat{u}^\dagger$) and are separately plotted in the figure.

The first term (——), depends only on the base flow values whereas the second term (- - -), depends only on the perturbation solved using LST. On comparing each individual term separately across all Ec, we observe that the first term has a positive value in the boundary layer with a peak ≈ 0.3 and is zero in the freestream. This term does not change significantly as Ec increases. Whereas, the second term which is positive for $Ec = 0.05$, reduces in magnitude before switching signs to contribute to a negative value for $Ec = 0.15$. Additionally for $Ec = 0.15$, the value of the second term is no longer zero in the freestream. This change in signs in the real part of the complex velocity product, from positive to negative, is hypothesised as the reason for a modally stable flow at high Ec.

This fundamental approach is only a hypothesis towards explaining the stability of the flows and is not yet verified.

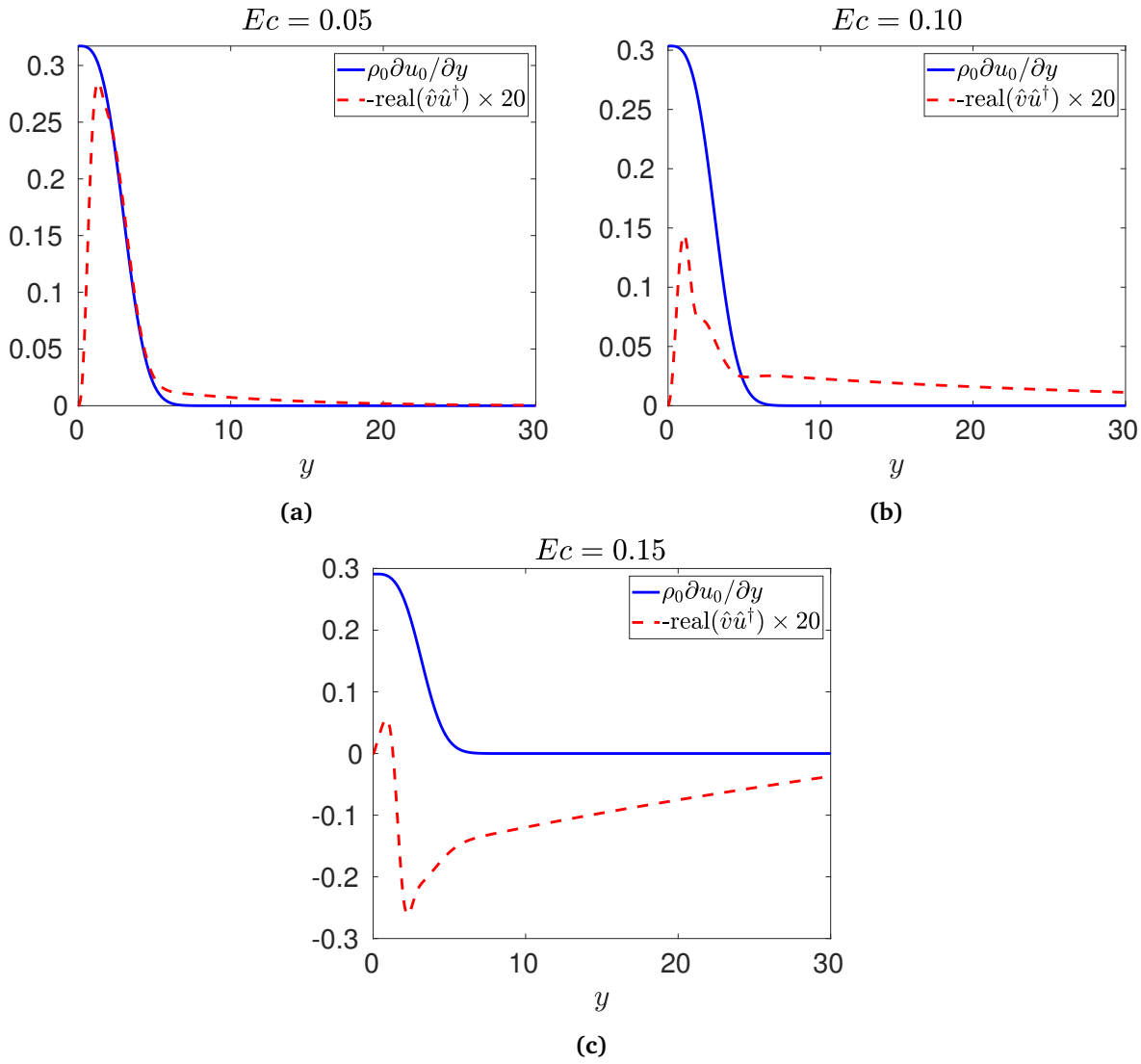

Figure 4.19: (a) Ec =0.05; (b) Ec = 0.10; (c) Ec = 0.15. Profiles of individual term contributing to the production of perturbation energy: $\rho_0 \partial u_0/y$ - - -and -real$(\hat{v}\hat{u}^\dagger)$ ——.

Chapter 5

Conclusions and recommendation

In the present work, a complete investigation of the stability of flows of toluene over a flat plate boundary layer has been conducted. The base flow and linear stability analysis have been performed for 6 different Eckert numbers, while the DNS results have been computed for 4 different Eckert numbers.

5.1 Concluding remarks

1. The base flow, linear stability and direct numerical simulations were successfully performed for flows with ideal-air and non-ideal toluene.
2. From the results of LST for flows of toluene and the subsequent validation using the DNS solver suggested that the non-ideal effects of toluene which manifest itself at high Ec **stabilise the flow completely**.
3. From the base flow, it was concluded that the freestream values were not affected by changing the values of Ec and its effects were only present within the boundary layer. The base flow profiles increased in gradient upon increasing the Eckert number, for both ideal air and toluene flows. The temperature base flow profiles are the same for both flows, but a difference was observed in the profiles of streamwise velocity, density, dynamic viscosity and thermal conductivity. The maximum deviation in the profiles between the fluids was observed for thermal conductivity followed by dynamic viscosity. This deviation is a manifestation of the non-ideal effects of toluene.
4. From the results in stability analysis, it was inferred that the effect of increasing Ec had a stabilising effect for both fluids. The stabilising effect of increasing Ec was very minute for ideal gas and very drastic for toluene. For the toluene cases, the **flows are modally stable at $Ec > 0.12$**. On checking the effect of the spanwise wavenumber on the neutral curve, it was found to reduce the size and shape of the neutral curve at $Ec = 0.05$, suggesting that the 2D mode is the most important mode of perturbation.
5. The DNS code was successfully adapted to run for any fluid whose properties are available in `Fluidprop` and subsequently verified for CO_2 and toluene.
6. Results of eigenfunctions, growth rate and phase velocity between linear stability and direct numerical simulations were compared for $Ec = 0.05$, 0.10 and 0.15. LST predicted strong growth for $Ec = 0.05$, a weak growth for $Ec = 0.10$ and no growth for $Ec = 0.15$. The DNS results match perfectly with LST for $Ec = 0.05$ and 0.10 in the growing region. The results between the LST and DNS deviate in stable regions due to a possibility of superposition of contributions of multiple decaying modes. This deviation

was observed to be the largest for $Ec = 0.15$. Both DNS and LST predict stable flows for flows greater than $Ec = 0.15$.

7. A perturbation energy analysis was performed for each case. It was found that the spatial growth of the perturbation are positive for $Ec = 0.05$ and 0.10 but is negative for $Ec = 0.15$. This is due to the negative contribution of the complex product $\hat{v}\hat{u}^{\dagger}$ suggesting a stabilising effect of a shear layer flows at higher Eckert numbers.

5.2 Recommendation

The work presented in this report is an initial attempt to understand the stability of flows of toluene over a flat plate. The work is still primitive and a large scope exists for future work.

1. The perturbations were analysed for 2D disturbances in a 2D domain. For a more complete analysis of stability, 3D domains for 2D and oblique modes could be performed for toluene at large Mach number.
2. The boundary conditions at wall was assumed to be adiabatic. The behaviour of the flow for an isothermal wall could also be investigated for a more wholesome understanding of toluene flows over a flat plate.
3. Linear stability analysis is shown to predict the DNS values very accurately for during growing flows but poorly for stable flows. This was hypothesised to be effect of superposition of multiple decaying modes. A validation of this hypothesis and a more fundamental understanding of why the LST and DNS results differ in stable regions could be conducted.
4. The work analysed flows over a simple flat plate. Analysis for more complicated geometries can be performed to check effects of curvature, roughness and non-parallelism among others.

Appendices

Appendix A

Fluid property table

The base flow, LST and DNS results for toluene cases are solved using properties taken from the `Fluidprop` library. 2 property tables were created for this purpose and the salient features of each table are explained here.

A.1 1D look-up table

The 1D look-up table is used primarily to evaluating the base flow. The 1D table is an `.dat` file comprising of 200 rows and 8 columns of data viz. entalpy h^*, temperature T^*, pressure P^*, density ρ^*, dynamic viscosity μ^*, specific heat capacity C_p^*, thermal conductivity κ^* and speed of sound c^*. The pressure is maintained at 1.8 bar, with the temperature increasing linearly from T = 410K upto T = 700 K. Figure A.1, plots the variation of density (A.1 a), dynamic viscosity (A.1 b), specific heat capacity (A.1 c) and thermal conductivity (A.1 d) as function of temperature alone. The plots are a representation of the data generated at constant pressure of 1.8 bar. It's observed from figure A.1, that the variation of each parameter is monotonically increasing or decreasing for an increase in temperature, with no discontinuities or inflection points. The density decreases non-linearly with increase in temperature whereas the viscosity, thermal conductivity and specific heat capacity all increase non-linearly with the increase of temperature.The reference state of each parameter is also indicated in the figure ($\star$).

The self-similar boundary layer equations are solved for ideal gas using the ideal gas equations with the viscosity computed according to Sutherland's law. No 1D table is required for its analysis. For toluene, the properties are taken directly from the 1D look-up table with suitable interpolations when required.

A.2 2D look-up table

The 2D look-up table is a 801×201 table containing values of temperature (T^*), gas constant (R^*), density (ρ^*), dynamic viscosity (μ^*), thermal conductivity (κ^*) and specific heat capacity (C_p^*). The table is a 2D matrix of varying e and ρe as required by the DNS code. The 2D table uses 800 values of e^* and 200 values of $\rho^* e^*$ and is generated using a `C++` code that reads and stores the required data from the `Fluidprop` database. The gas constant (R^*) in the table is a replacement for pressure and is calculated as $R^* = P^*/\rho^* T^*$.

Figure A.2, provides a visual representation of the 2D look-up table using contour plots of pressure, temperature, thermal conductivity and specific heat capacity with ρe on the y-axis and e on the x-axis.

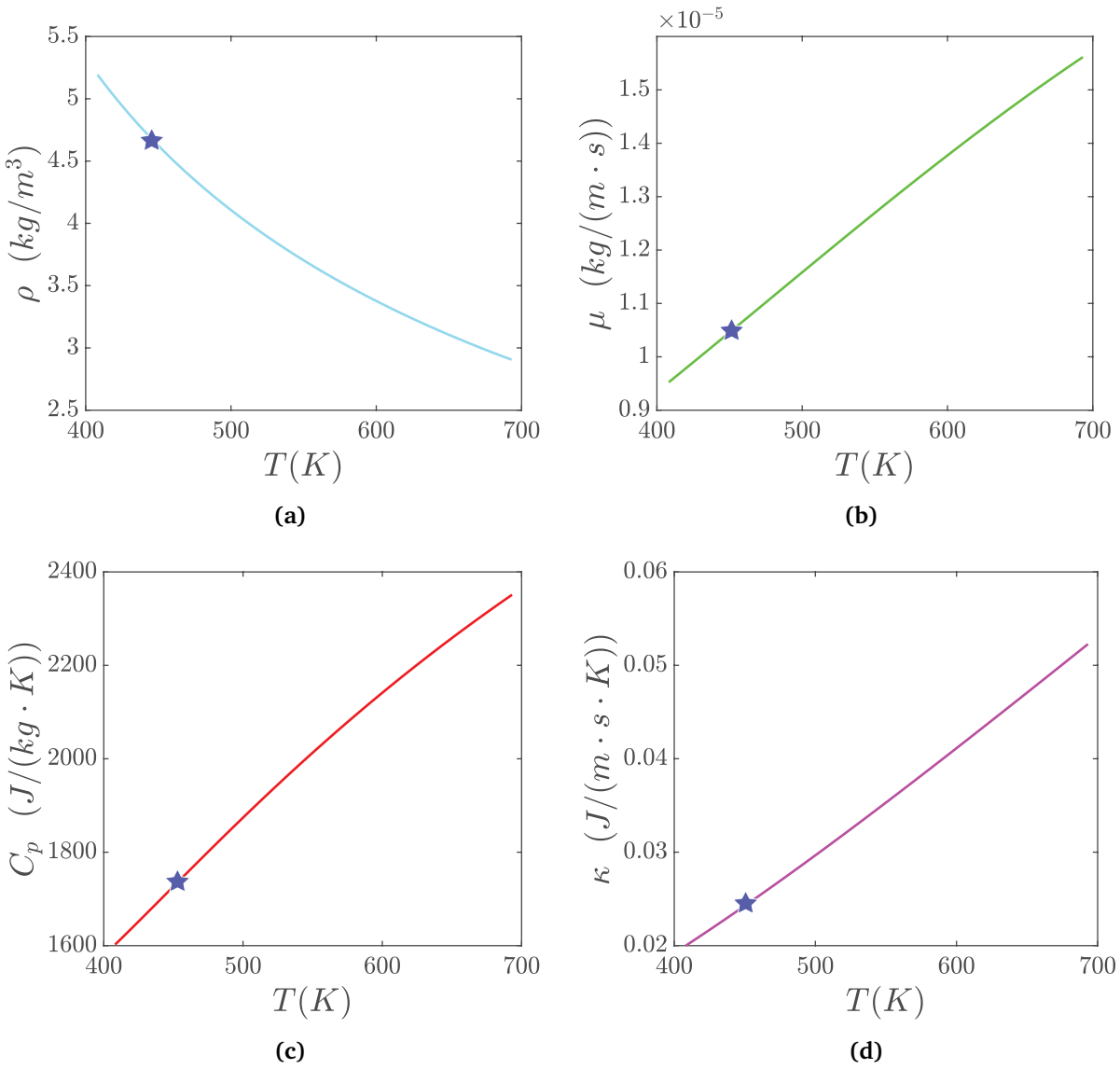

Figure A.1: (a) Density profile; (b) Dynamic viscosity profile; (c) Specific heat capacity profile; (d) Thermal conductivity profile. Representation of the 1D look-up table by plotting various properties as a function of temperature. The reference state of the problem in indicated using a ($\star$) in the each plot.

The isobar of 1.8 bar (white curve) along with the reference state ($\star$) is indicated for each contour plot to provide an insight of the values of each property within the computation domain.

The range of the 2D table is chosen carefully, ensuring it covers the expected pressures P^* and temperature T^* ranges, the fluid would have across domain of the flow. Values when the fluid enter the 2 phase region or exceeds the limits of the data available within the database are set to -888888. For a well chosen limits of e^* and $\rho^* e^*$, such negative values should be avoided in the data generated and thereby prevent bad inputs to the DNS simulation.

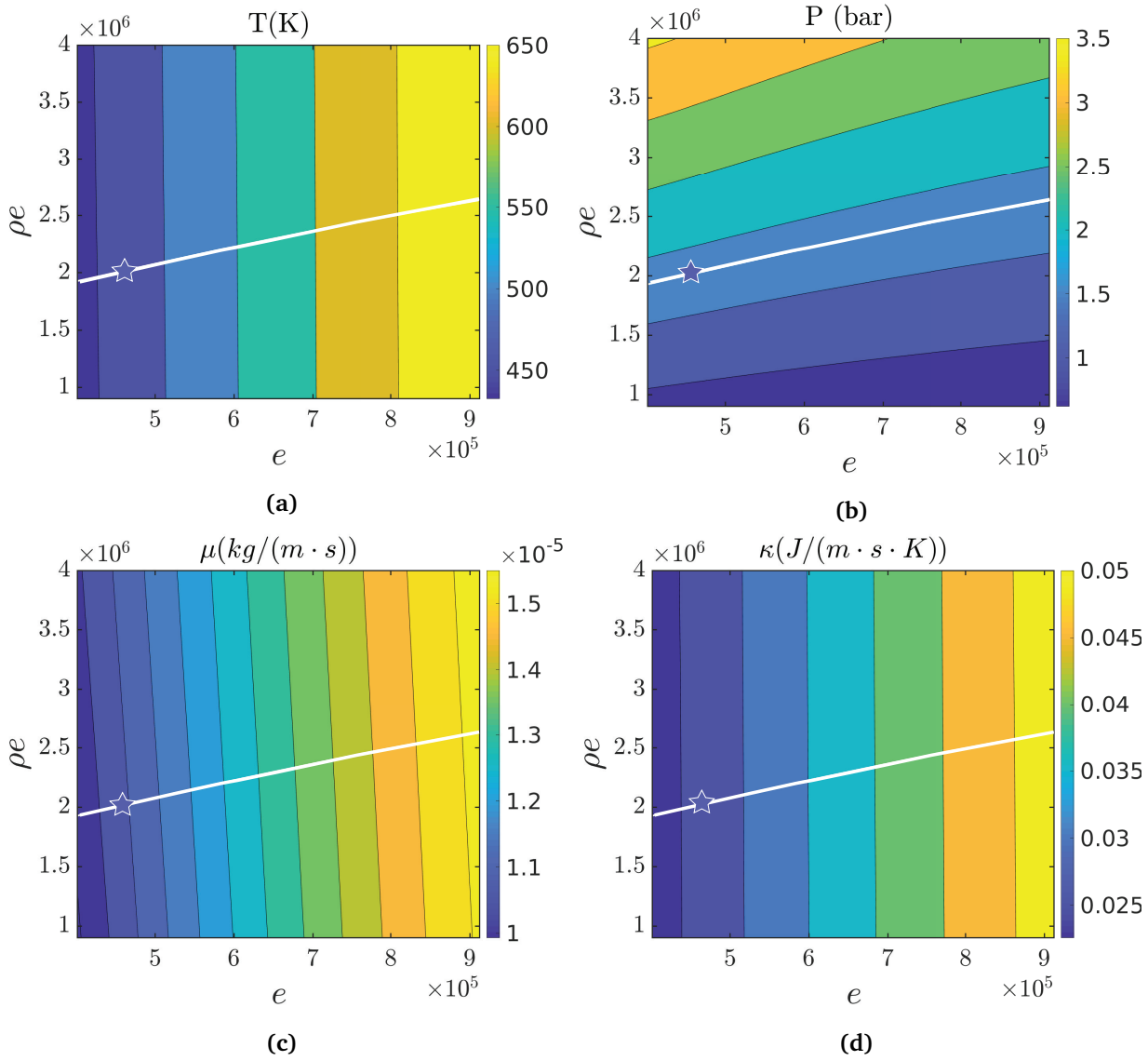

Figure A.2: (a) Contours of temperature; (b) Contours of pressure, (c) Contours of dynamic viscosity; (d) Contours of thermal conductivity. Visualisation of the 2D look-up table as a function of ρe and e. The reference state of the problem is indicated using a ($\star$) and the isobar p= 1.8 bar is indicated with a white curve.

Appendix B

Perturbation energy analysis

For a more fundamental understanding of the mechanisms of instability growth in non-ideal fluids, a perturbation energy analysis and subsequently an energy budget analysis can be performed. The perturbation energy balance equation is derived from the stability equations by adding the x-momentum perturbation equation (multiplied throughout with $\hat{u}^\dagger$) and the y-momentum perturbation equation (multiplied with $\hat{v}^\dagger$). The dagger represents the complex conjugate of the term. Substituting the growth of density in the x-momentum equation using the continuity equations and simplifying the terms and grouping we get the following kinetic energy balance equation:

$$\Theta = P + K + T + V, \tag{B.1}$$

where

$$\Theta = -i\alpha \int \rho_0 u_0 (\hat{u}\hat{u}^\dagger + \hat{v}\hat{v}^\dagger) dy, \tag{B.2}$$

$$K = -i\omega \int \rho_0 (\hat{u}\hat{u}^\dagger + \hat{v}\hat{v}^\dagger) dy, \tag{B.3}$$

$$P = -\int \rho_0 \frac{\partial u_0}{\partial y} \hat{v}\hat{u}^\dagger dy, \tag{B.4}$$

$$\begin{aligned} T = -\int \Bigg[& i\alpha \frac{\partial p_0}{\partial \rho_0} \hat{\rho}\hat{u}^\dagger + i\alpha \frac{\partial p_0}{\partial T_0} \hat{T}\hat{u}^\dagger + \frac{\partial p_0}{\partial \rho_0} \frac{\partial \hat{\rho}}{\partial y} \hat{v}^\dagger + \frac{\partial p_0}{\partial T_0} \frac{\partial \hat{T}}{\partial y} \hat{v}^\dagger + \\ & \left(\frac{\partial^2 p_0}{\partial \rho_0^2} \frac{\partial \rho_0}{\partial y} + \frac{\partial^2 p_0}{\partial \rho_0 \partial T_0} \frac{\partial T_0}{\partial y} \right) \hat{\rho}\hat{v}^\dagger + \left(\frac{\partial^2 p_0}{\partial T_0^2} \frac{\partial T_0}{\partial y} + \frac{\partial^2 p_0}{\partial \rho_0 \partial T_0} \frac{\partial \rho_0}{\partial y} \right) \hat{T}\hat{v}^\dagger \Bigg] dy, \end{aligned} \tag{B.5}$$

$$
\begin{aligned}
V = \frac{1}{Re}\int \Bigg[& -\alpha^2 (2\mu_0 + \lambda_0)\hat{u}\hat{u}^\dagger + \mu_0 \frac{\partial^2 \hat{u}}{\partial y^2}\hat{u}^\dagger + i\alpha(\mu_0 + \lambda_0)\frac{\partial \hat{v}}{\partial y}\hat{u}^\dagger \\
& + i\alpha \frac{\partial \mu_0}{\partial y}\hat{v}\hat{u}^\dagger + \frac{\partial \mu_0}{\partial \rho_0}\frac{\partial u_0}{\partial y}\frac{\partial \hat{\rho}}{\partial y}\hat{u}^\dagger + \frac{\partial \mu_0}{\partial y}\frac{\partial \hat{u}}{\partial y}\hat{u}^\dagger + \frac{\partial \mu_0}{\partial T_0}\frac{\partial u_0}{\partial y}\frac{\partial \hat{T}}{\partial y}\hat{u}^\dagger \\
& + \frac{\partial \mu_0}{\partial \rho_0}\frac{\partial^2 u_0}{\partial y^2}\hat{\rho}\hat{u}^\dagger + \frac{\partial u_0}{\partial y}\left(\frac{\partial^2 \mu_0}{\partial \rho_0^2}\frac{\partial \rho_0}{\partial y} + \frac{\partial^2 \mu_0}{\partial \rho_0 \partial T_0}\frac{\partial T_0}{\partial y}\right)\hat{\rho}\hat{u}^\dagger \\
& + \frac{\partial \mu_0}{\partial T_0}\frac{\partial^2 u_0}{\partial y^2}\hat{T}\hat{u}^\dagger + \frac{\partial u_0}{\partial y}\left(\frac{\partial^2 \mu_0}{\partial T_0^2}\frac{\partial T_0}{\partial y} + \frac{\partial^2 \mu_0}{\partial T_0 \partial \rho_0}\frac{\partial \rho_0}{\partial y}\right)\hat{T}\hat{u}^\dagger \\
& - \alpha^2 \mu_0 \hat{v}\hat{v}^\dagger + (2\mu_0 + \lambda_0)\frac{\partial^2 \hat{v}}{\partial y^2}\hat{v}^\dagger + i\alpha(\mu_0 + \lambda_0)\frac{\partial \hat{u}}{\partial y}\hat{v}^\dagger \\
& + i\alpha \frac{\partial \mu_0}{\partial \rho_0}\frac{\partial u_0}{\partial y}\hat{\rho}\hat{v}^\dagger + i\alpha \frac{\partial \lambda_0}{\partial y}\hat{u}\hat{v}^\dagger + i\alpha \frac{\partial \mu_0}{\partial T_0}\frac{\partial u_0}{\partial y}\hat{T}\hat{v}^\dagger + \left(2\frac{\partial \mu_0}{\partial y} + \frac{\partial \lambda_0}{\partial y}\right)\frac{\partial \hat{v}}{\partial y}\hat{v}^\dagger \Bigg] dy.
\end{aligned}
\tag{B.6}
$$

The real part of each term within equation (B.1), together constitute the balance of the energy given to the perturbations. Θ_r signifies the contributions of spatial growth of the perturbation energy, K_r signifies the contributions due to the temporal growth and does not contribute to the spatial problem due to a purely imaginary value of K, P_r refers to the production term, T_r is the thermodynamic term and V_r is the viscous dissipation. An examination of the contribution of each term towards the spatial growth of the perturbation is referred to as the energy budget analysis and is a powerful tool to comment on the nature of the instabilities within the flow.

Appendix C

Additional results for toluene flows with $Ec = 0.45$

Apart from the results presented in section 4.4, results of LST and DNS were also compared for $Ec = 0.45$. This case has a Mach number of 2.9639, which is closer to the Mach number in the stator of an ORC turbines. The results for these cases are given in figure C.1. In figure C.1a, it is observed that for $Ec = 0.45$, both LST and DNS show a stable flow. the results of DNS have wiggles but seem to match accurately with the predictions from LST. On comparing the phase velocities (figure C.1b), we observe that the phase velocities are in the same order-of-magnitude till $x = 10$, after which the DNS results jump to a phase velocity of 1.3 throughout the domain.

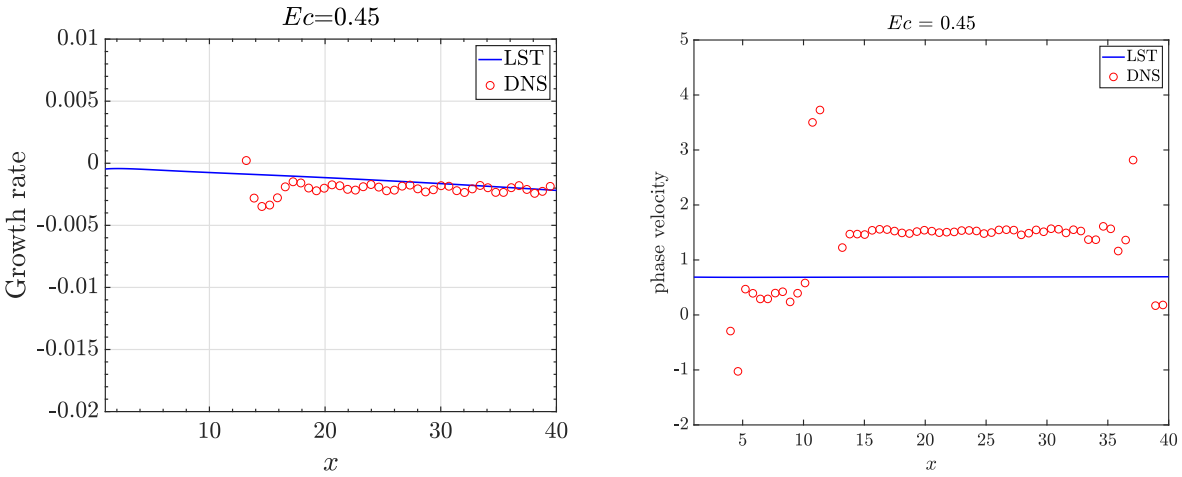

(a) **(b)**

Figure C.1: (a) Growth rate for $Ec = 0.45$; (b) phase velocity for $Ec = 0.45$. Comparison between the results obtained from DNS ∘ and the results predicted by LST —.

A phase velocity greater than unity suggest the behaviour due to mode F modes with a negative growth rate, but no such mode exists in the eigenvalue spectrum. Comparing the Eigenfunctions at $x = 7$ (figure C.2a) and $x = 25$ (figure C.2b), we can clearly observe no qualitative or quantitaive match in between the results of DNS and LST. This is in line with the results observed in section 4.4, where an increase in Ec, made the flow modally stable and increased the deviation between LST and DNS.

Thus at $Ec = 0.45$, the LST is incapable of predicting the behaviour of DNS. This could be due to the presence of effects such as **non-parallel effects** or rapid changes in streamwise values which the LST is unable to identify.

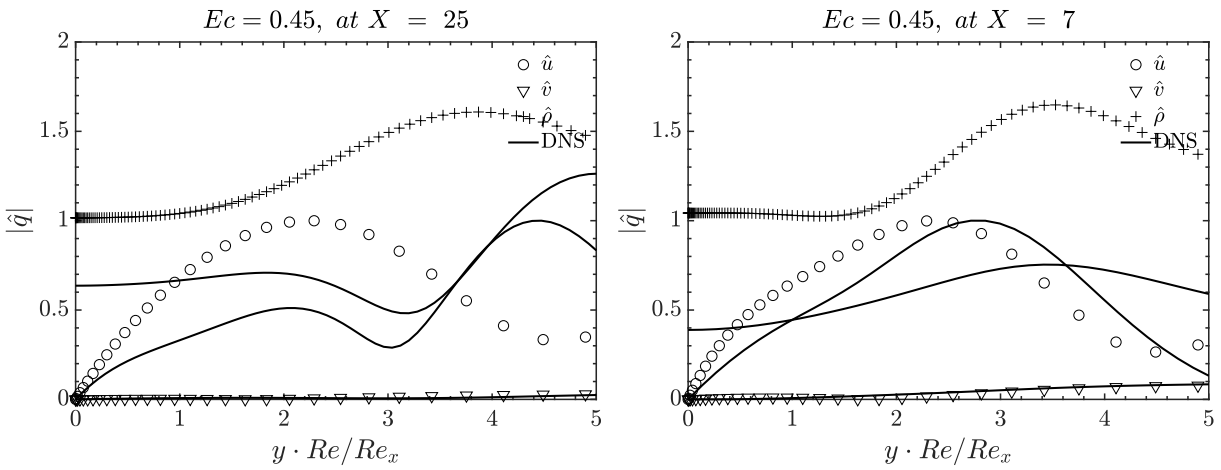

(a) **(b)**

Figure C.2: (a) Eigenfunctions at $x = 7$; (b) Eigenfunctions at $x = 25$. Comparison between eigenfunctions from DNS and corresponding plots of magnitude of perturbations in streamwise $\circ$, wall normal velocity $\bigtriangledown$ and density $+$ as predicted by LST for $Ec = 0.45$.

Bibliography

[1] Red and black smoke. https://wallpaper-gallery.net/single/red-and-black-smoke-background-10.html, Accessed: 2018-09-05.

[2] J. Anderson Jr. Hypersonic and high temperature gas dynamics, 2000.

[3] H. Blasius. Uber grenschichten in flüssigkeiten bei sehr kleiner reisbung. *Zeitschr. f. Math. u. Phys*, 56(1), 1908.

[4] A. V. Boiko, A. V. Dovgal, G. R. Grek, and V. V. Kozlov. *Physics of Transitional Shear Flows: Instability and Laminar–Turbulent Transition in Incompressible Near-Wall Shear Layers*, volume 98. Springer Science & Business Media, 2011.

[5] A. Demetriades. Hypersonic viscous flow over a slender cone. iii-laminar instability and transition. In *7th Fluid and PlasmaDynamics Conference*, page 535, 1974.

[6] A. Dorodnitsyn. Laminar boundary layer in compressible fluid. In *Dokl. Akad. Nauk SSSR*, volume 34, pages 213–219, 1942.

[7] D. Dunn. On the stability of the laminar boundary layer in a compressible fluid. *Journal of the Aeronautical Sciences*, 22(7):455–477, 1955.

[8] A. Fedorov. Transition and stability of high-speed boundary layers. *Annual review of fluid mechanics*, 43:79–95, 2011.

[9] M. Gaster. A note on the relation between temporally-increasing and spatially-increasing disturbances in hydrodynamic stability. *Journal of Fluid Mechanics*, 14(2):222–224, 1962.

[10] M. Gaster. On the effects of boundary-layer growth on flow stability. *Journal of Fluid Mechanics*, 66(3):465–480, 1974.

[11] P. Germain and H. Hornung. Transition on a slender cone in hypervelocity flow. *Experiments in Fluids*, 22(3):183–190, 1997.

[12] N. Gregory, J. T. Stuart, and W. Walker. On the stability of three-dimensional boundary layers with application to the flow due to a rotating disk. *Phil. Trans. R. Soc. Lond. A*, 248(943): 155–199, 1955.

[13] F. H. Harlow and J. E. Welch. Numerical calculation of time-dependent viscous incompressible flow of fluid with free surface. *The physics of fluids*, 8(12):2182–2189, 1965.

[14] H. G. Hornung. Hypersonic real-gas effects on transition. In *IUTAM Symposium on One Hundred Years of Boundary Layer Research*, pages 335–344. Springer, 2006.

[15] M. L. Hudson, N. Chokani, and G. V. Candler. Linear stability of hypersonic flow in thermochemical nonequilibrium. *AIAA journal*, 35(6):958–964, 1997.

[16] R. D. Joslin. Aircraft laminar flow control. *Annual review of fluid mechanics*, 30(1):1–29, 1998.

[17] J. Kendall. Wind tunnel experiments relating to supersonic and hypersonic boundary-layer transition. *AIAA Journal*, 13(3):290–299, 1975.

[18] L. Lees. Laminar heat transfer over blunt-nosed bodies at hypersonic flight speeds. *Journal of Jet Propulsion*, 26(4):259–269, 1956.

[19] L. Lees and H. Gold. Stability of laminar boundary layers and wakes at hypersonic speeds. part i. stability of laminar wakes. *Fundamental phenomena in hypersonic flow*, (4):310–337, 1964.

[20] L. Lees and E. Reshotko. Stability of the compressible laminar boundary layer. *Journal of Fluid Mechanics*, 12(4):555–590, 1962.

[21] S. K. Lele. Compact finite difference schemes with spectral-like resolution. *Journal of computational physics*, 103(1):16–42, 1992.

[22] S. Levy. Effect of large temperature changes (including viscous heating) upon laminar boundary layers with variable free-stream velocity. *Journal of the Aeronautical Sciences*, 21(7):459–474, 1954.

[23] C.-H. Ling and W. Reynolds. Non-parallel flow corrections for the stability of shear flows. *Journal of Fluid Mechanics*, 59(3):571–591, 1973.

[24] L. Mack. Jet propulsion laboratory report no. 900-277 rev, 1969.

[25] L. M. Mack. Boundary-layer linear stability theory. Technical report, California Inst. of Tech Pasadena Jet Propulsion Lab, 1984.

[26] M. Malik and E. Anderson. Real gas effects on hypersonic boundary-layer stability. *Physics of Fluids A: Fluid Dynamics*, 3(5):803–821, 1991.

[27] O. Marxen, G. Iaccarino, and E. S. Shaqfeh. Disturbance evolution in a mach 4.8 boundary layer with two-dimensional roughness-induced separation and shock. *Journal of Fluid Mechanics*, 648: 435–469, 2010.

[28] O. Marxen, T. Magin, G. Iaccarino, and E. S. Shaqfeh. A high-order numerical method to study hypersonic boundary-layer instability including high-temperature gas effects. *Physics of Fluids*, 23(8):084108, 2011.

[29] F. K. Moore. Three-dimensional boundary layer theory. In *Advances in Applied Mechanics*, volume 4, pages 159–228. Elsevier, 1956.

[30] M. V. Morkovin. Critical evaluation of transition from laminar to turbulent shear layers with emphasis on hypersonically traveling bodies. Technical report, Martin Marietta Corp. Baltimore MD Research Inst. for Advanced Studies, 1969.

[31] S. Nagarajan, S. K. Lele, and J. H. Ferziger. A robust high-order compact method for large eddy simulation. *Journal of Computational Physics*, 191(2):392–419, 2003.

[32] W. M. Orr. The stability or instability of the steady motions of a perfect liquid and of a viscous liquid. part ii: A viscous liquid. In *Proceedings of the Royal Irish Academy. Section A: Mathematical and Physical Sciences*, pages 69–138. JSTOR, 1907.

[33] S. B. Pope. Turbulent flows, 2001.

[34] L. Prandtl. Bemerkungen über die entstehung der turbulenz. *ZAMM-Journal of Applied Mathematics and Mechanics/Zeitschrift für Angewandte Mathematik und Mechanik*, 1(6): 431–436, 1921.

[35] L. Rayleigh. On the stability, or instability, of certain fluid motions. *Proc. London Math. Soc.*, 9: 57–70, 1880.

[36] J. Ren, S. Fu, and R. Pecnik. Linear instability of poiseuille flows with highly non-ideal fluids. *Journal of Fluid Mechanics*, in press.

[37] E. Reshotko. *Stability of three-dimensional compressible boundary layers*, volume 1220. National Aeronautics and Space Administration, 1962.

[38] E. Reshotko. Boundary-layer stability and transition. *Annual Review of Fluid Mechanics*, 8(1): 311–349, 1976.

[39] O. Reynolds. An experimental investigation of the circumstances which determine whether the motion of water shall he direct or sinuous, and of the law of resistance in parallel channels. *Philosophical Transactions of the Royal Society of London*, 174:935–982, 1883.

[40] N. S. *Leading edge effects in bypass transition*. PhD thesis, Stanford university, 2004.

[41] V. H. Schlichting. Laminare strahlausbreitung. *ZAMM-Journal of Applied Mathematics and Mechanics/Zeitschrift für Angewandte Mathematik und Mechanik*, 13(4):260–263, 1933.

[42] P. J. Schmid and D. S. Henningson. *Stability and transition in shear flows*, volume 142. Springer Science & Business Media, 2012.

[43] G. B. Schubauer and H. K. Skramstad. Laminar-boundary-layer oscillations and transition on a flat plate. Technical report, NATIONAL AERONAUTICS AND SPACE ADMINISTRATION WASHINGTON DC, 1948.

[44] D. H. Sharp. Overview of rayleigh-taylor instability. Technical report, Los Alamos National Lab., NM (USA), 1983.

[45] A. Sommerfeld. Ein beitrag zur hydrodynamischen erklaerung der turbulenten fluessigkeitsbewegungen. *Atti del*, 4:116–124, 1908.

[46] H. B. Squire. On the stability for three-dimensional disturbances of viscous fluid flow between parallel walls. *Proc. R. Soc. Lond. A*, 142(847):621–628, 1933.

[47] G. Stuckert and H. L. Reed. Linear disturbances in hypersonic, chemically reacting shock layers. *AIAA Journal*, 32(7):1384–1393, 1994.

[48] P. A. Thompson. A fundamental derivative in gasdynamics. *The Physics of Fluids*, 14(9): 1843–1849, 1971.

[49] P. A. Thompson and K. Lambrakis. Negative shock waves. *Journal of Fluid Mechanics*, 60(1): 187–208, 1973.

[50] W. Tollmien, D. M. Miner, et al. The production of turbulence. Technical report, National Advisory Committee for Aeronatutics Langley Field VA Langley Aeronautical Laboratory, 1931.

[51] L. N. Trefethen. Finite difference and spectral methods for ordinary and partial differential equations. 1996.

[52] C. Zamfirescu, A. Guardone, and P. Colonna. Admissibility region for rarefaction shock waves in dense gases. *Journal of Fluid Mechanics*, 599:363–381, 2008.